Icarus 286 (2017) 69–93

Contents lists available at ScienceDirect

Icarus

journal homepage: www.elsevier.com/locate/icarus

How the martian residual south polar cap develops quasi-circular and heart-shaped pits, troughs, and moats

Peter B. Buhler[a,*], Andrew P. Ingersoll[a], Bethany L. Ehlmann[a,b], Caleb I. Fassett[c], James W. Head[d]

[a] California Institute of Technology, Department of Geological and Planetary Science, Pasadena, CA 91125, USA
[b] Jet Propulsion Laboratory, California Institute of Technology, Pasadena, CA 91109, USA
[c] Mount Holyoke College, Department of Astronomy, South Hadley, MA 01075, USA
[d] Brown University, Department of Geological Sciences, Providence, RI 02912, USA

ARTICLE INFO

Article history:
Received 25 July 2016
Available online 13 January 2017

ABSTRACT

The martian Residual South Polar Cap (RSPC) is a 1–10 m thick deposit of permanent CO_2 ice perched on the much larger H_2O ice cap. The CO_2 ice is dissected into mesas by erosional landforms that can be broadly classified as (i) quasi-circular pits, (ii) heart-shaped pits, (iii) linear troughs, and (iv) moats. We use HiRISE (25–50 cm/px) images taken at a cadence of days to months to track meter-scale changes in the RSPC in order to investigate the mechanisms that lead to the development of these four distinct morphologies.

For the first time, we report the development of dark fans on the sides of the CO_2 mesas and the fracturing and deterioration of the initially smooth upper surface of CO_2 mesas. We interpret these features as indicating the sublimation and subsequent escape of CO_2 from the interiors of mesas, which undermines structural support of mesa tops, causing them to collapse. The collapse of mesa tops, along with uneven deposition of CO_2 ice, creates steep scarps that erode during the summer due to preferential sunlight absorption. During the winter, CO_2 deposition acts to smooth topography, creating gently sloping ramps. We propose that the interplay between the steep scarps and gentle slopes leads to either quasi-circular pits, heart-shaped pits, linear troughs, or moats, depending on local conditions.

1. Introduction

Huygens made the first recorded sketch of a bright south polar spot on Mars in 1672 (Sheehan, 1996), and additional notable observations of the martian south pole were made by Maraldi, Herschel, and Schroeter in the eighteenth century, leading Herschel to propose that Mars hosted northern and southern polar ice caps (Herschel, 1784; Sheehan, 1996). These early observers did not know the composition or structure of these caps but did note that they changed seasonally, indicating that they were primarily observing the seasonal polar caps. In the mid-twentieth century, Leighton and Murray (1966) proposed that the caps were a reservoir composed entirely of CO_2 in equilibrium with the atmosphere, but, over the next few decades, others presented evidence and later demonstrated that the residual summertime north polar ice is entirely H_2O, and that the residual summertime south polar ice deposit is predominantly a $\sim 10^6$ year old (Herkenhoff and Plaut, 2000), $2–3 \times 10^6$ km^3 deposit made of H_2O ice (e.g. Ingersoll, 1974; Durham et al., 1999; Smith et al., 1999; Nye et al., 1999; Byrne and Ingersoll, 2003; Titus et al., 2003). Radar observations of the south polar ice (Phillips et al., 2011) have subsequently revealed that a $\sim 10^4$ km^3 CO_2 ice reservoir (i.e. a mass of CO_2 similar to the mass of the current, 96% CO_2 atmosphere (Owen et al., 1977)) with an age of $\sim 10^5$ year is entombed within the H_2O ice at a depth of <20 m (Bierson et al., 2016), reviving the concept of an equilibrium between the atmosphere and a comparably large, solid CO_2 reservoir, albeit on longer than annual timescales. No permanent CO_2 reservoirs have been observed in the northern hemisphere.

In this paper we present observations and interpretations of annual and seasonal changes in the residual south polar cap (RSPC; a.k.a. unit Aa_{4b} (Tanaka et al., 2007, 2014)). The RSPC is a 1–10 m thick CO_2 ice deposit that has a mass of ~1% of the present-day atmosphere (Thomas et al., 2016) that overlies the mostly inert H_2O ice and buried CO_2 deposit just described. It is the only known CO_2 deposit in contact with the atmosphere that has a general

* Corresponding author.
E-mail addresses: bpeter@caltech.edu, sagax13@gmail.com (P.B. Buhler).

http://dx.doi.org/10.1016/j.icarus.2017.01.012

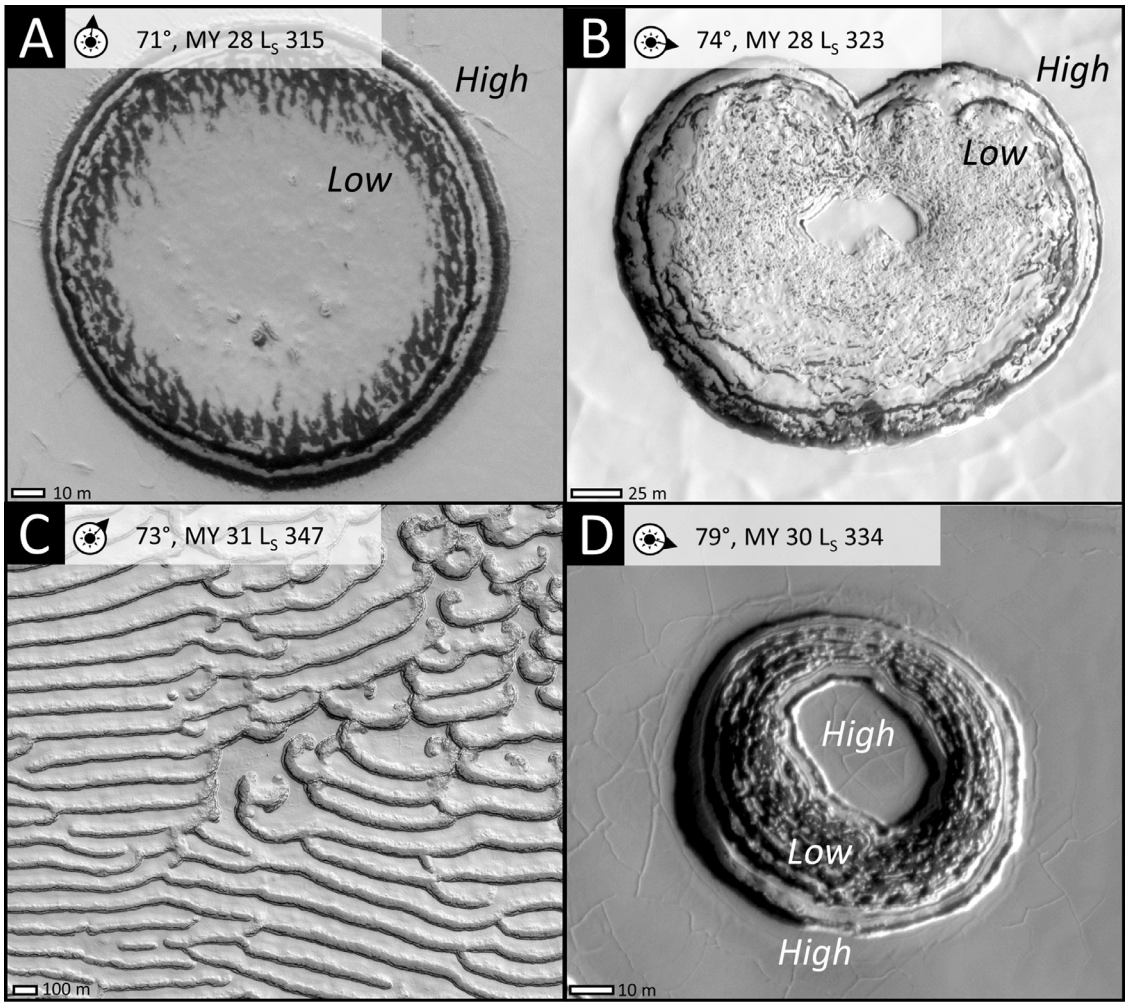

Fig. 1. a. Quasi-circular pit. b. Heart-shaped pit (note cusp). c. A field of linear troughs. d. A smooth-topped mesa surrounded by a low-elevation, rough moat, contained wholly within another smooth-topped mesa. Selected high (H) and low (L) terrains are marked as an aid to the eye. HiRISE images (A) PSP_005349_0930 (B) PSP_005517_0930 (C) PSP_006007_0925 (D) ESP_023410_0930.

structure that is stable intra- and inter-annually. Each winter a ~1 m-thick seasonal deposit of CO_2 ice blankets the southern pole, including the RSPC (e.g., Piqueux et al., 2015), but this seasonal deposit sublimates entirely each summer (e.g., Hess et al., 1979; James et al., 1992). The RSPC as a whole appears quasi-stable on decadal timescales.

The RSPC consists of plateaus and mesas of CO_2 ice that are dissected by myriad pits and troughs, which typically change annually at meter-scales (e.g. Malin et al., 2001). Most of these morphologies have been extensively documented (Thomas et al., 2005, 2009, 2013, 2016), although a comprehensive understanding of how these landforms develop has remained elusive. In the published literature, the growth of quasi-circular pits has been shown to occur through the erosion of their steep walls via sublimation and calving (e.g. Byrne and Ingersoll, 2003), which has been modeled by Byrne et al. (2008, 2015). However, a description of the inception of quasi-circular pits and of the systematic development of the other CO_2-ice dissection morphologies has not been promulgated.

Before describing landform development and endeavoring to understand the mechanisms leading to the development of the morphology of the RSPC, we first direct the reader to Fig. 1, a visual definition of the terminology used here and in the literature to describe the four main categories of landforms dissecting the RSPC: quasi-circular pits, heart-shaped pits, linear troughs, and moats (see also Thomas et al., 2016). Most of these terms are self-evident, but we specifically note that 'moat' describes the lower elevation, non-smooth region surrounding a smooth-topped mesa that is wholly within another smooth-topped mesa.

Understanding the mechanisms leading to the variety of morphologies in the RSPC is not only intrinsically interesting, but also important to our understanding of the martian climate in general, since current climate models do not predict the existence of the RSPC (e.g. Guo et al., 2009). Understanding the processes governing the development of the RSPC, therefore, likely provides insight into the past and future of the martian climate and into the processes leading to the development of the much larger buried CO_2 deposit.

Documenting the mechanisms of meter-scale morphologic changes is challenging because it is difficult to find clear examples of morphologic change that have repeated coverage at high cadence. However, there are now five consecutive martian years of 25–50 cm/px coverage of some locations on the RSPC by the High Resolution Imaging Science Experiment (HiRISE) camera (McEwen et al., 2007), which makes the problem tractable. We therefore use these data to infer the processes leading to the emergence of the multitude of morphologic forms of the RSPC.

2. Methods

We use 25–50 cm/px images from the HiRISE camera on board the Mars Reconnaissance Orbiter (McEwen et al., 2007) to

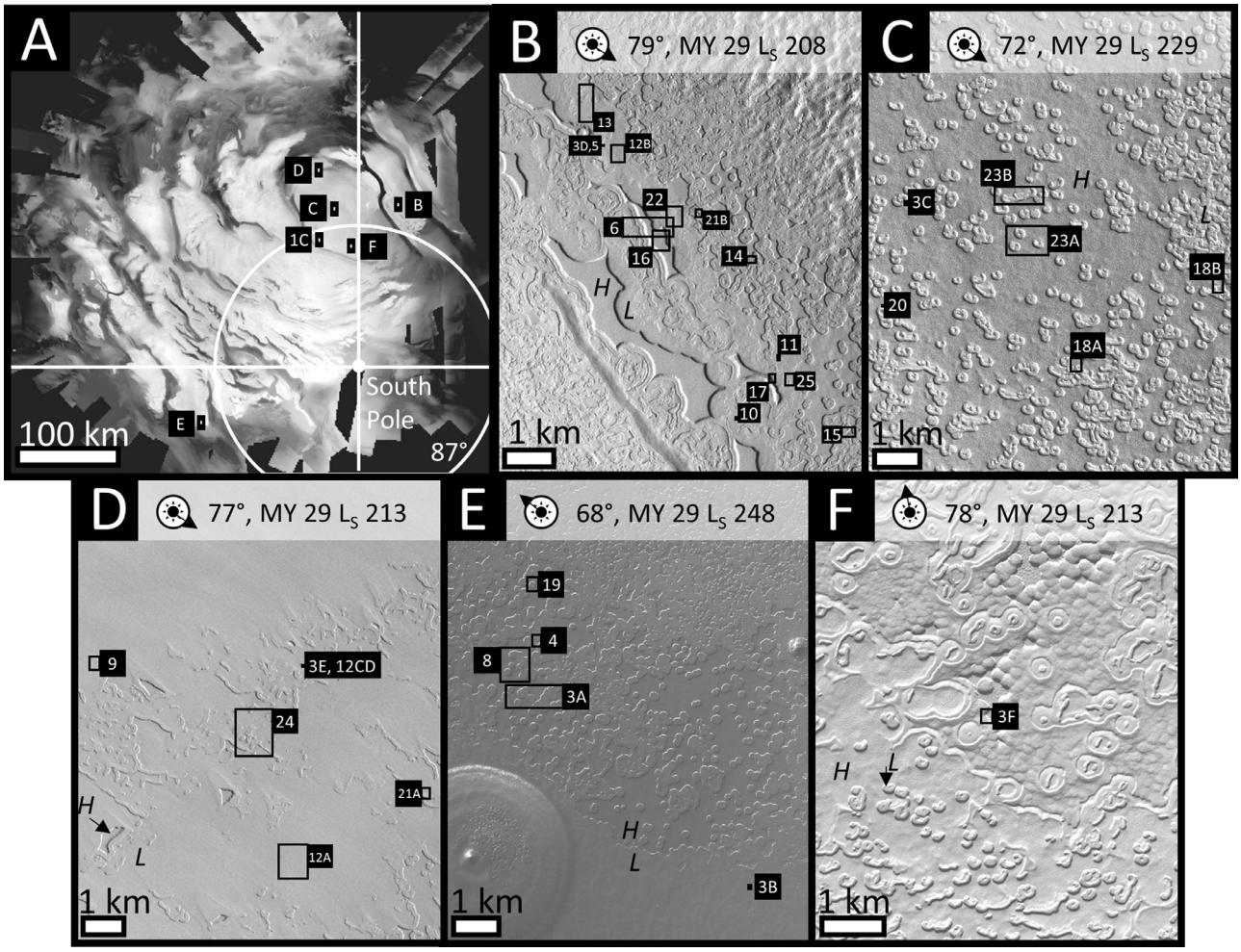

Fig. 2. Context images for other figures (labeled black boxes). Units that appear in the image are given in the caption (based upon Thomas et al., 2016). a. Mosaic of CTX images taken in southern spring MY 29, showing context for panels b–f and Fig. 1c. White boxes give the true sizes of panels b–f relative to panel a, black outline provides visual clarity of the locations. b. Units A0 and Un. c. Unit A1. d. Units B2 and B8. e. Unit B7. f. Unit C1. CTX images (B) B06_011951_0933 (C) B07_012374_0931 (D) B06_012044_0945 (E) B08_012760_0933 (F) CTX B06_012047_0884; (A) is a mosaic of CTX images.

document the morphology at five locations on the RSPC at a cadence of, at best, 4 sols between images. The maximum number of HiRISE images obtained from any single study location in any particular Mars Year was 11, while some study areas have no HiRISE coverage during some Mars Years. We made use of a total of 95 HiRISE images. The selected locations cover seven different units of the RSPC, including units representing each of the three broader unit groups A, B, and C (as defined by Thomas et al. (2016)) in order to sample spatially distinct and morphologically diverse regions of the RSPC (Fig. 2). We refer to the units using the nomenclature from Thomas et al., (2016), and 'Un' refers specifically to the 'unmapped' portion of the RSPC in the box approximately bounded by ([10 E, −86.6 N], [13 E, −86.5 N], [21 E, −87 N], [23 E, −86.9 N]) (Fig. 2b).

Images were imported with martian polar stereographic projection and co-registered in ArcMap 10 onto a basemap constructed from Mars Reconnaissance Orbiter Context Camera images (Malin et al., 2007). Repeat images were finely co-registered by hand at each location using multiple fiducial points, such as the polygonal pattern on the H_2O ice basement. We estimate that the accuracy between images is within ~1 pixel over features of interest. In all images illumination direction is indicated by a sun symbol, followed by the solar incidence angle (solar elevation measured from a normal to the surface), Mars Year, and Solar Longitude (L_S, where L_S is 0° at the vernal equinox, 90° at summer solstice, 180° at autumnal equinox, and 270° at winter solstice). Most HiRISE images shown in figures are contrast enhanced in order to highlight subtle features; the contrast stretch is the same for all images within the same figure. Photogrammetry was used to determine the vertical offset of features on mesa tops by using measurements of the length of shadows cast by the fractures in HiRISE images with low-angle solar illumination.

3. Observations

We observe the intra- and inter-annual development of RSPC morphology, describing features and processes not previously documented: (i) dark fans emanating from mesa sides; (ii) fracturing and (iii) collapse of mesa tops; and the initiation and evolution of (iv) quasi-circular and (v) heart-shaped pits, troughs, and moats.

3.1. Dark fans on mesa sides

During southern spring, dark fans with typical surface areas of ~1–10 m^2 ubiquitously appear on the sides and bases of the RSPC CO_2 mesas (Figs. 3 and 4). The darkest and narrowest segment of fans is located closest to the mesa side, and fans become gradationally lighter moving away from the mesa side. Occasionally, fans are draped over the sides and onto the upper surface of the mesas (Fig. 3b). Over tens of sols, areas with fans become uniformly dark

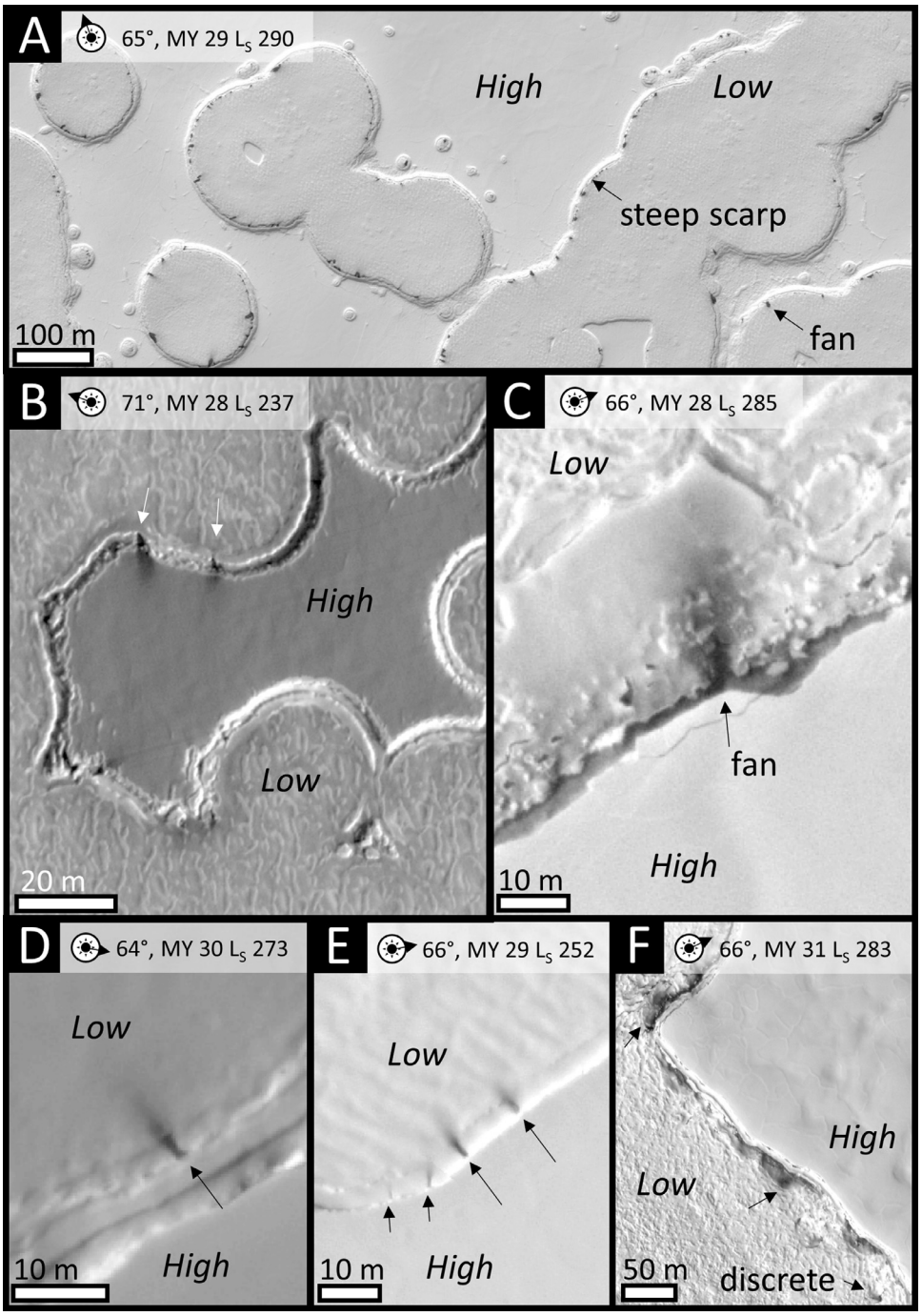

Fig. 3. Examples of fans from all five study locations. a. Unit B7. Dark fans appear exclusively near the edges of CO_2 mesas. b. Unit B7. Dark fans on the upper surface of a mesa. c. Unit A1. Close-in view of typical fan morphology. d. The Un. e. Unit B2. f. Unit C1. Note both discrete fans and broad dark band. HiRISE images (A) ESP_013617_0930 (B) PSP_0,03716_0930 (C) PSP_004687_0930 (D) ESP_022210_0930 (E) ESP_012835_0940 (F) ESP_031099_0925.

as underlying seasonal CO_2 frost preferentially sublimates (Fig. 5). By mid-summer it is no longer possible to distinguish fans from underlying terrain, which has darkened (Fig. 6b and c).

The timing of dark fan appearance is typically during southern spring, prior to L_S 240, but varies slightly by location and by unit (Fig. 7). The earliest fans are apparent in the first images of Unit A0 in Mars Year (MY) 28, at solar longitude (L_S) 184. However, the Un, which appears in the same images, does not have fans until L_S 195 in MY 28. Additionally, although Unit A1 has coverage at L_S 201 in MY 28, the first fans do not appear in images until L_S 221.

The rate of fan formation varies by location, with the highest spatial density of dark fans found in Unit B7. The lowest density of discrete dark fans is found in Unit C1, although broad, equal elevation, dark bands appear around the edges of mesas within Unit C1 (Fig. 3f) and Unit A0 (Fig. 8a).

The number of dark fans formed per year martian year varies within our study areas in Units B7, A0, and the Un, with more dark fans appearing in Mars Year (MY) 29 than in MY 28 and 31 (e.g., Fig. 8). However, variation in the annual rate of dark fan formation in other units cannot be confidently determined, due to lack of sufficient spatial and temporal coverage.

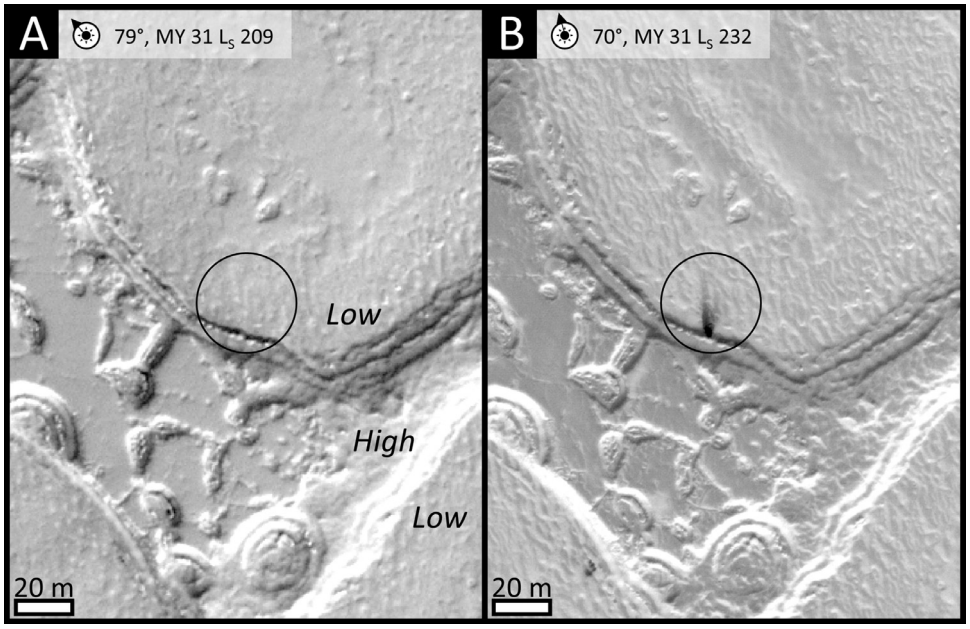

Fig. 4. Unit B7. a. No dark fan. b. 38 sols later. Dark fan is apparent. HiRISE images (A) ESP_029586_0930 (B) ESP_030073_0930.

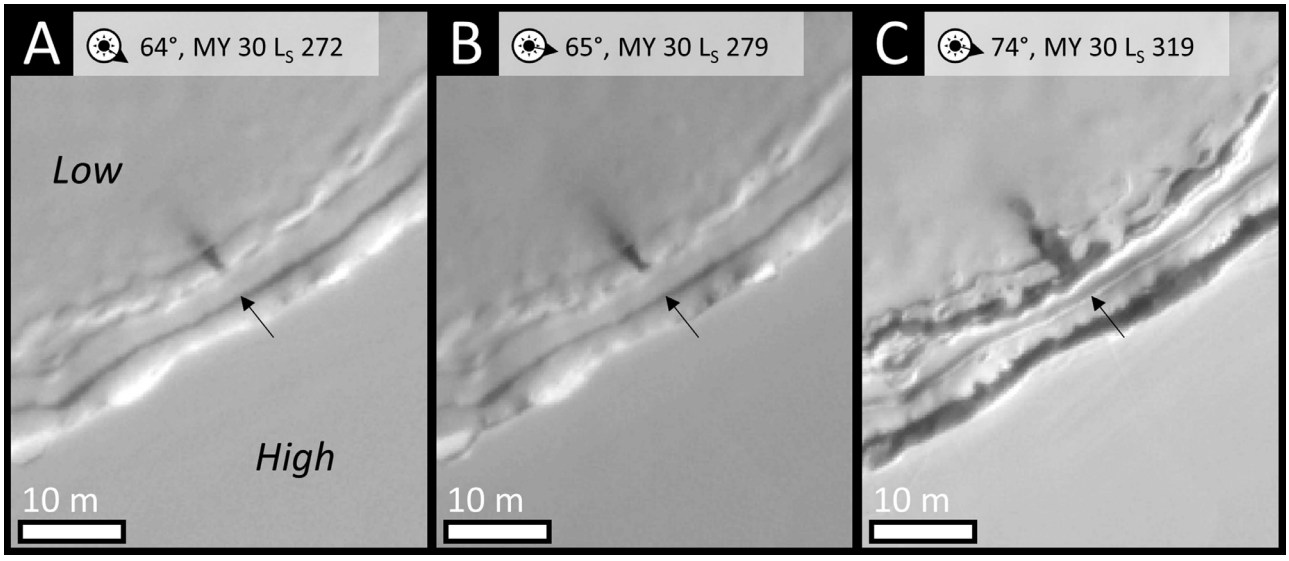

Fig. 5. The Un. a. Dark fan at the base of a CO_2 mesa. b. 12 sols later. c. 77 sols later. Seasonal frost has begun to sublimate completely, revealing underlying dark material. Note preferential sublimation at the location of the fan. HiRISE images (A) ESP_022064_0930 (B) ESP_022210_0930 (C) ESP_023054_0930.

3.2. Fracturing of mesa upper surfaces

In our study areas mesas typically have a bright, tens-of-centimeter-thick upper surface layer overlying a darker interior (as measured from HiRISE images, e.g. Fig. 6b and c). Thin fractures with a vertical offset of ~10 ± 3 cm (determined from photogrammetry) and a lateral extent of ~10–100 m occur on the upper surface of this bright layer in Units B2, C1, and the Un (Figs. 9–11). Fractures often appear to be the boundary between two vertically offset slabs (Figs. 10 and 11). Some fractures have a single sense of offset (Figs. 9 and 10), but others have a scissoring offset, i.e., the offset direction changes along the strike of the fracture (Fig. 11). The fractures sometimes occur in isolation (Figs. 9–11) and sometimes in clusters (Fig. 10).

In MY 32, some newly formed fractures viewed after L_S 320 exhibit bright halos with a radius of ~2–4 m on either side of a crack, highlighting the outlines of polygonal slabs, which have areas of 10^4–10^5 m^2 (Fig. 12a and b). In MY 28, some new fractures are also bright, but with less pronounced halos than those in MY 32 (Fig. 12c and d; black arrow). However, fractures with halos are restricted to portions of mesas that, based on shadow measurements of bounding scarps, are only between ~0.5 - 2 m thick. New fractures on thicker parts of mesas occur without halos in the same scenes (Fig. 13).

The earliest new fractures are observed by L_S 249 and continue to appear until at least L_S 299 (Fig. 7). New fractures have not been observed in Units A0 and A1, despite extensive imaging coverage, and there is insufficient coverage to determine whether new fractures form in Units B7 and B8.

Fractures initially have a crisp scarp, which is retained until the end of summer (Figs. 9–11). By the following spring, the edge is typically muted, and, in subsequent summers, the fractures

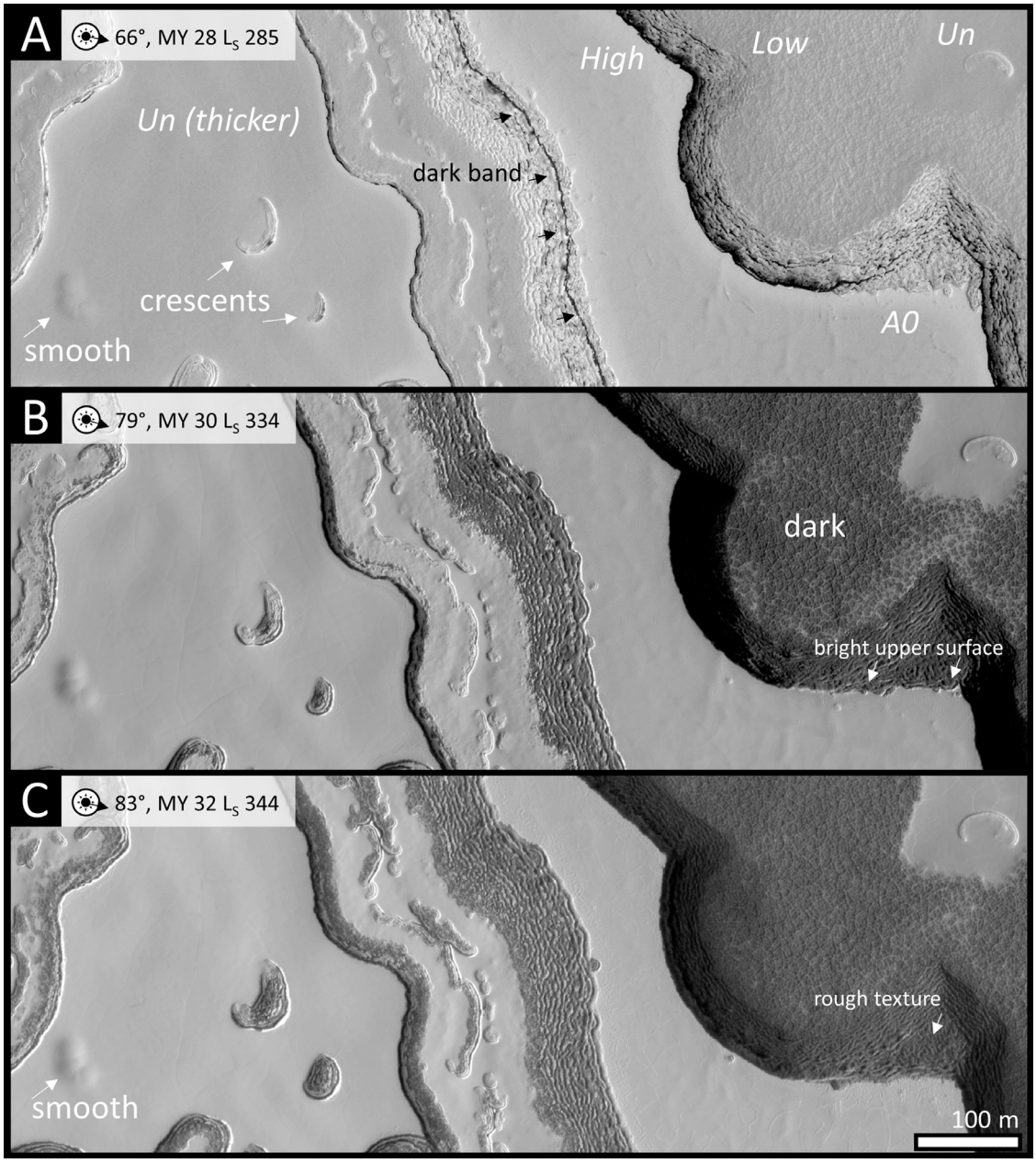

Fig. 6. Unit A0 and Un (labeled in image). 5 martian year time series at different L_S. a. Note dark band, smooth depression, and crescents. b. Note dark polygonal basement, dark sides of mesa and L_S. Also note that the thickness of bright upper surface (white arrows) is a few tens of centimeters. The height of the entire mesa is 10 m (based on shadow measurements). c. Smooth depression (lower left corner) has not evolved. Crescents in thicker region of Un (left side) have enlarged more than crescent in thinner Un deposit (upper right). Note dark, rough texture below bright upper surface. HiRISE images (A) PSP_004686_0930, (B) ESP_023410_0930, (C) ESP_041278_0930.

can (i) maintain a single-ridged morphology (Fig. 11, 3rd panel), (ii) develop a double-ridged morphology (Fig. 11, 4th panel), or (iii) become strongly muted and almost invisible (Fig. 11, 5th panel). The progression from an initially crisp offset to an increasingly muted offset is typical of the newly forming fractures we observe.

Ridges in regions of the RSPC will sometimes re-crack, forming wider cracks (Fig. 14b, c, f, i). Re-cracking has been observed as early as L_S 248 and continues until at least L_S 319. Re-cracking preferentially occurs within ~10–40 m of meters of mesa edges bounded by steep scarps (Fig. 14i). The upper surface of the mesa within ~10–40 m of the mesa edges also tends to be lower than the central region, when bounded by a steep scarp, and lowering of the edges appears to accompany re-cracking (Fig. 15b).

3.3. Collapse and deterioration of upper mesa surfaces

Flat-bottomed polygonal depressions with areas on the order of 10^2 m^2, with $\sim 10 \pm 3$ cm of relief (determined from photogrammetry), and typically 3–6 sides develop on the upper surfaces of mesas in mid- to late summer (Figs. 14d, i and 16). The edges of the polygonal depressions tend to be coincident with ridges (Figs. 14d and 16), and, in areas within ~10–40 m of the mesa edge, ridges typically re-crack before polygonal depressions appear (Fig. 14b and c). The polygonal depressions form abruptly, in the span of ≤ 4 sols (Fig. 16). By late summer, large fields of adjacent polygons form; the largest fields can comprise up to several hundred polygons and have areas of up to 10^5 m^2 (Fig. 16). The fields of polygons can cover nearly the entirety of the upper surface of mesas in Unit A0 (Fig. 16), but tend to be restricted to the edges

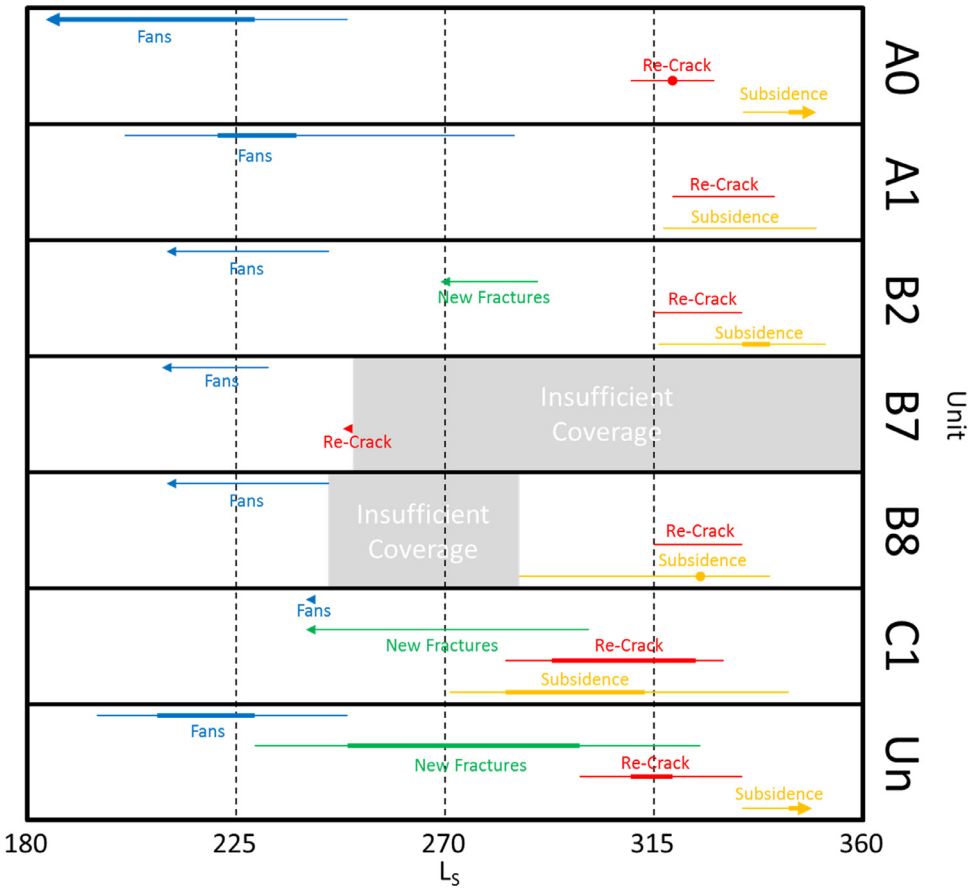

Fig. 7. Seasonal timing of different features by unit. Thin lines represent the interval between an image with no new features and an image in which new features have appeared (i.e. maximum activity duration). Thick lines represent the interval between two images that each have new features appearing (i.e. minimum activity duration). Arrows indicate that new features are present in the first or the final image of a particular year. "Insufficient Coverage" indicates low temporal cadence of high-quality images. All intervals are constructed between images taken in the same martian year. For features that have sufficient coverage in more than one year to construct intervals, the interval shown in this figure spans the interval from both years (i.e., making the interval longer). Since many locations have sufficient coverage of a particular morphologic phenomenon to construct intervals in only one martian year, it is not yet practical to compare seasonal timing of features between years. Note: no new fractures were observed in Units A0 or A1.

of mesas in thinner units (e.g. Fig. 14i). Polygonal depressions develop by L_S 283 and continue to form until at least L_S 349 (Fig. 7). Polygonal depressions are observed in every unit except B7, though this may be due to a lack of coverage of B7 in late summer.

As an example, we show the development and evolution of polygons in the Un (Fig. 14). During the spring following polygon formation, the raised ridges between the polygons are muted, but still present in positive relief (Fig. 14e). By late the next summer, the boundaries between polygons within ~10–40 m of the sides of the mesa re-crack (Fig. 14f) and, two martian years later, have negative relief and have either developed a shallow single trough (Fig. 16d) or double-trough morphology (Fig. 14g and h). On the other hand, after two martian years, the boundaries between polygons that are more than ~40 m from the edges of the mesa still have muted positive relief (e.g., Fig. 16d, in unit A0).

Polygonal depressions were observed to form in MY 28 in Units B2 and B8, MY 30 in Units A0, A1, C1, and the Un, and MY 31 in Units B2, B8, and C1. In most cases, there is insufficient late-summer coverage of the same locations in other years to determine whether polygons form again. However, in A0 and in the Un, polygonal depressions do not form twice in the same location during MY 28–31 within the entirety of the area shown in Fig. 2b.

Near the sheer edges of thick mesas, particularly in locations where high mesas become thin in planform, the bright, smooth upper surface sometimes deteriorates, revealing an underlying vermicular texture (Fig. 17). As the upper surface deteriorates, thin, bright, linear ridges parallel to the edges of the retreating upper surface are usually evident. The interior of the mesa is immediately dark once the smooth upper surface disappears.

3.4. Inception of quasi-circular pits

Some fractures have points of collapse ~1–2 m in radius that become the inception locations of quasi-circular pits (Fig. 18a), while other fractures widen into a quasi-circular pit (Fig. 19, a_1). In both cases, we measure that the steep scarps that encompass the pits erode at a rate of ~2 m/martian year by sublimation over the five martian years of observations. This is similar to the erosion rates observed for larger pits by Thomas et al. (2005, 2009). The smallest pit we observe that exhibits erosion via calving blocks on its walls has a radius of ~10 m (Fig. 20).

3.5. Gentle ramps and steep scarps combine to form heart-shaped pits, linear troughs, and moats

In some cases, crescentic features develop instead of circular pits. In one typically observed case, a portion of a collapsing area along a fracture remains attached to the upper surface of the mesa, forming a crescentic pit: a pit that has a smooth ramp abutting a steep scarp (Fig. 18b). The same crescentic morphology also develops in ~5 m-wide alcoves that occur at the termini of gentle slopes of CO_2 ice (Fig. 21a). Additionally, surface irregularities on smooth

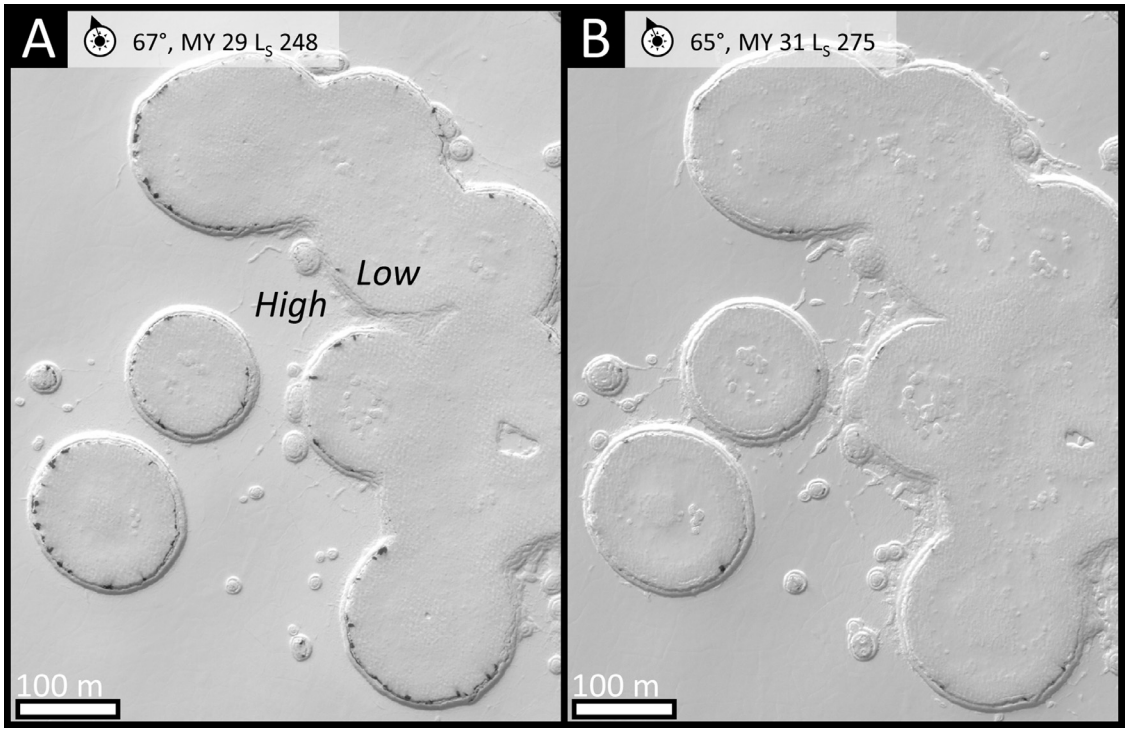

Fig. 8. Unit B7. a. More fans are apparent in MY 29 earlier in summer. b. Fewer fans are apparent in MY 31 later in summer. This is the closest timing (seasonality) in images available of this area comparing MY 29 and MY 31. HiRISE images (A) ESP_012760_0930 (B) ESP_030944_0930.

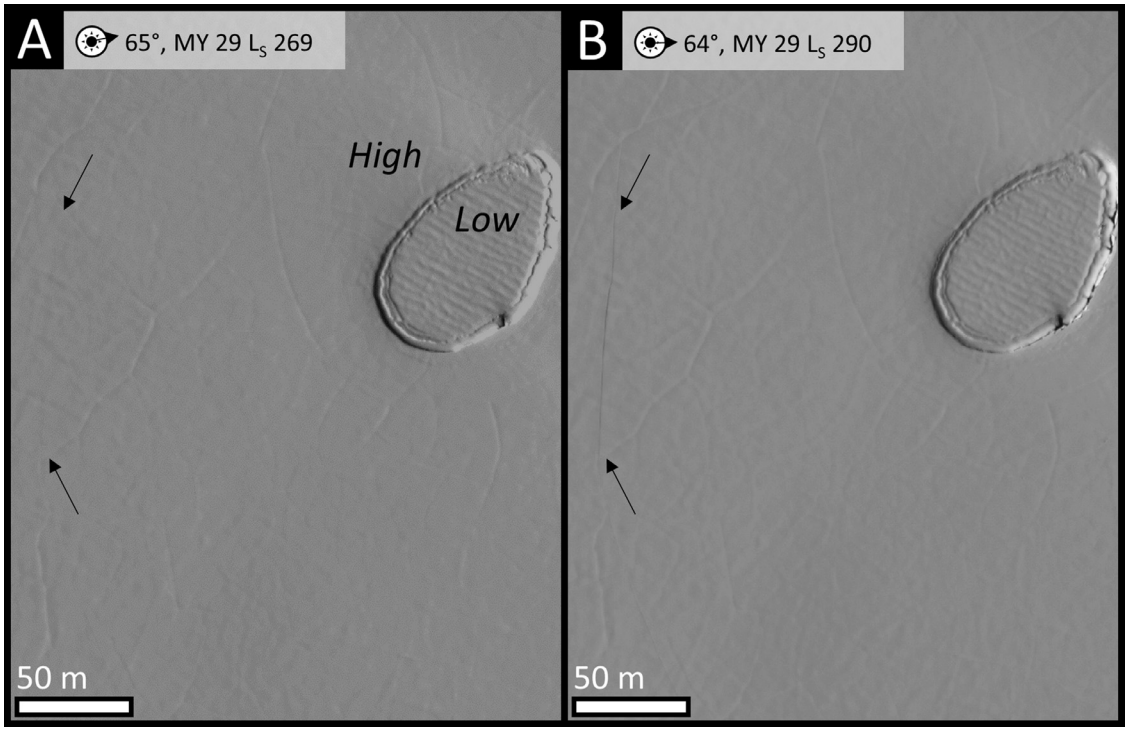

Fig. 9. Unit B2. Two images taken under nearly identical viewing conditions. a. MY 29 L_S 269 with solar incidence angle 65°, phase angle 63°, and emission angle 2.1° b. 34 sols later, MY 29 L_S 289.8, with solar incidence angle 66°, phase angle 66°, and emission angle 0.5° Crack appears. Note unchanged background pattern of thin ridges throughout scene. HiRISE images (A) ESP_013178_0940 (B) ESP_013613_0940.

ramps can develop into new, crescentic pits (Fig. 22), while small crescents sometimes disappear between summer and the spring of the following year (Fig. 21b).

Crescentic pits evolve along one of two different paths. In one scenario, the steep scarp may erode into the smooth ramp, dissecting it and forming a cusp, leading to a heart-shape. In this case, the portion of the ramp cut off from the upper surface becomes an isolated smooth-topped mesa within the pit, i.e., a moat forms (Fig. 23a). When many crescentic pits are in close proximity, the steep scarps of different pits can intersect, forming sinuous ridges, cusps, and moats (Fig. 24). In the second scenario, crescents also evolve into linear troughs when the smooth ramp instead expands

Fig. 10. The Un. Inset. The same area of the upper surface of the mesa as shown in the main panel is smooth 32 sols earlier. Main. Fractures and tilted slabs have appeared on the upper surface of the CO_2 mesa. Arrows point to the same locations in both the main and inset panels. HiRISE images (Inset) ESP_013731_0930 (Main panel) ESP_013309_0930.

laterally, encroaching onto the steep scarp (Figs. 23b and 24). Note that heart-shaped pits and linear troughs are intimately associated (Figs. 2c, 23b and 24).

Steep scarps in crescentic pits in our study areas erode at ~2 m/martian year, but the smooth ramp often remains abutting the steep scarp for the entire five-martian-year span of our observations (Figs. 18b and 22d–g), thus indicating that the horizontal extent of the smooth ramp is also increasing. Smooth ramps on the edges of mesas also increase in extent between martian years. Fig. 25 shows two smooth ramps initially separated by ~10 m merge together over the course of two martian years, yielding a growth rate of ~2.5 m/martian year on each scarp edge, although the magnitude of growth appears to vary locally during different Mars years.

4. Discussion

4.1. Mesa dust content generates dark fans

The morphology and seasonality of dark fans associated with the RSPC is similar to that of the dark fans seen in the seasonal CO_2 ice deposits on the araneiform ('spider-like') terrain in the cryptic region of the south polar cap (e.g. Kieffer, 2003, 2007; Kieffer et al., 2006; Piqueux et al., 2003; Hansen et al., 2010). This suggests that the dark fans on the sides of RSPC mesas likewise form from the deposition of (dark) dust lofted by a pressurized gas jet rupturing a sintered layer of CO_2 ice (see, e.g., Kieffer et al., 2006; Kieffer, 2007; Hansen et al., 2010). The fact that some dark fans drape over the top of CO_2 mesas (Fig. 3b) also indicates such an explosive deposition process.

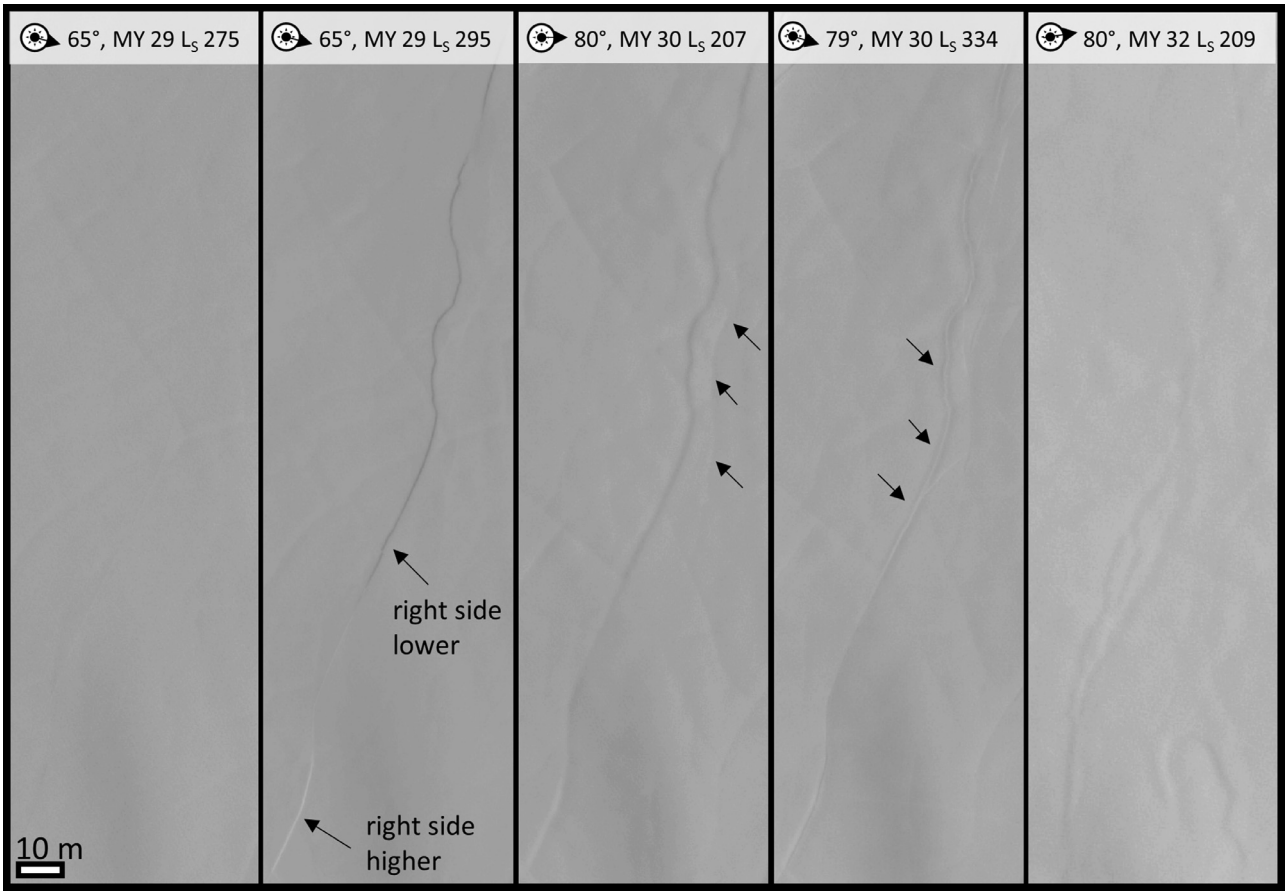

Fig. 11. The Un. Time series from left to right. i. Smooth upper surface of mesa. ii. Fracture with a vertical offset appears. iii. MY 30 spring. Crack is muted. Note second, approximately parallel, ridge (arrows). iv. MY 30 summer. Fracture has a double-ridged morphology (arrows). v. MY 32 spring. Ridge is strongly muted. HiRISE images (A) ESP_013309_0930 (B) ESP_013731_0930 (C) ESP_020733_0930 (D) ESP_023410_0930 (E) ESP_038403_0930.

In this scenario, the mesa must be sealed by an outer confining layer strong enough to at least temporarily confine the pressurized gas. Deposition and subsequent annealing (Eluszkiewicz, 1993; Kieffer, 2007) of a layer of CO_2 blanketing the RSPC mesas during the winter would readily create such a confining layer, as discussed for seasonal CO_2 ice by Portyankina et al. (2012). The crisp edges of the fractures that appear on the upper surface of RSPC mesas (Figs. 9-11) indicate that the upper surface of the RSPC mesas undergo brittle failure, which is consistent with impermeable, annealed CO_2 ice. CO_2 deposited onto the sloped, uneven surface of the mesa sides (e.g. Fig. 6a) or near the angled intersection between the mesa sides and mesa base (e.g. Fig. 3a) would have more imperfections and weaknesses than CO_2 deposited onto the generally smooth mesa tops. This would make it easier for pressurized gas to break through mesa sides and would explain why fans are observed on the sides but not on the tops of mesas.

Dust falling onto the CO_2 ice will migrate downward through the ice (Kieffer, 2003, 2007), creating a layer of nearly pure ice overlying dirtier ice (Portyankina et al., 2010). This is consistent with our observations that the edges of mesas turn dark in summer, with an overlying tens-of-centimeters-thick layer of bright material (Fig. 6b and c). The interiors of mesas are also immediately dark once the upper surface deteriorates (Fig. 17). Dusty ice will absorb sunlight much more readily than clean ice and thus drive sublimation of CO_2 ice in mesa interiors, leading to pressurized gas, similar to how fans are thought to form in the seasonal CO_2 ice (e.g. Kieffer, 2003, 2007). Fans may appear earlier in the season on the sides of Unit A0 than on the Un because they are taller and will therefore intercept more sunlight in early spring, when the sun is low on the horizon.

The length of the fans emanating from RSPC mesas allows us to estimate the pressure sourcing the vents by comparing to models of the CO_2 gas geysers rupturing the seasonal CO_2 ice. Thomas et al. (2011) use a comprehensive fluid dynamic model to calculate that dust entrained in the geysers in the seasonal ice reaches heights of ~20–80 m with source pressures of $\sim 10^3$ Pa. This is slightly longer than the typical fan lengths on mesa sides ($<\sim$10 m; Fig. 3), suggesting similar or slightly lower pressures within the mesas. Due to differences in geometry and latitudinal differences between our study sites and the locations modeled by Thomas et al. (2011), it is difficult to compare the RSPC fans directly to the Thomas et al. (2011) models, but $< \sim 10^3$ Pa lies within the yield stresses of H_2O Ice I and Ice II ($\sim 10^2$–10^4 Pa; the yield stress of CO_2 ice is unknown; Portyankina et al. (2010)). Given the similarity between the fans we observe on the side of mesas and the fans modeled by Thomas et al. (2011), we conclude that pressures of $\sim < 10^3$ can be contained within the mesas, but fan formation on the sides of mesas could be modeled in more detail.

Fans do not develop in the seasonal CO_2 ice deposit between the RSPC CO_2 mesas, as they do in the seasonal deposits elsewhere on the south pole (Hansen et al., 2010; Portyankina et al., 2012). We speculate that this may be due to a lack of a mobile dust source on the H_2O ice basement—perhaps because it is blown away by wind—and thus no darkening agent. Consequently, even if

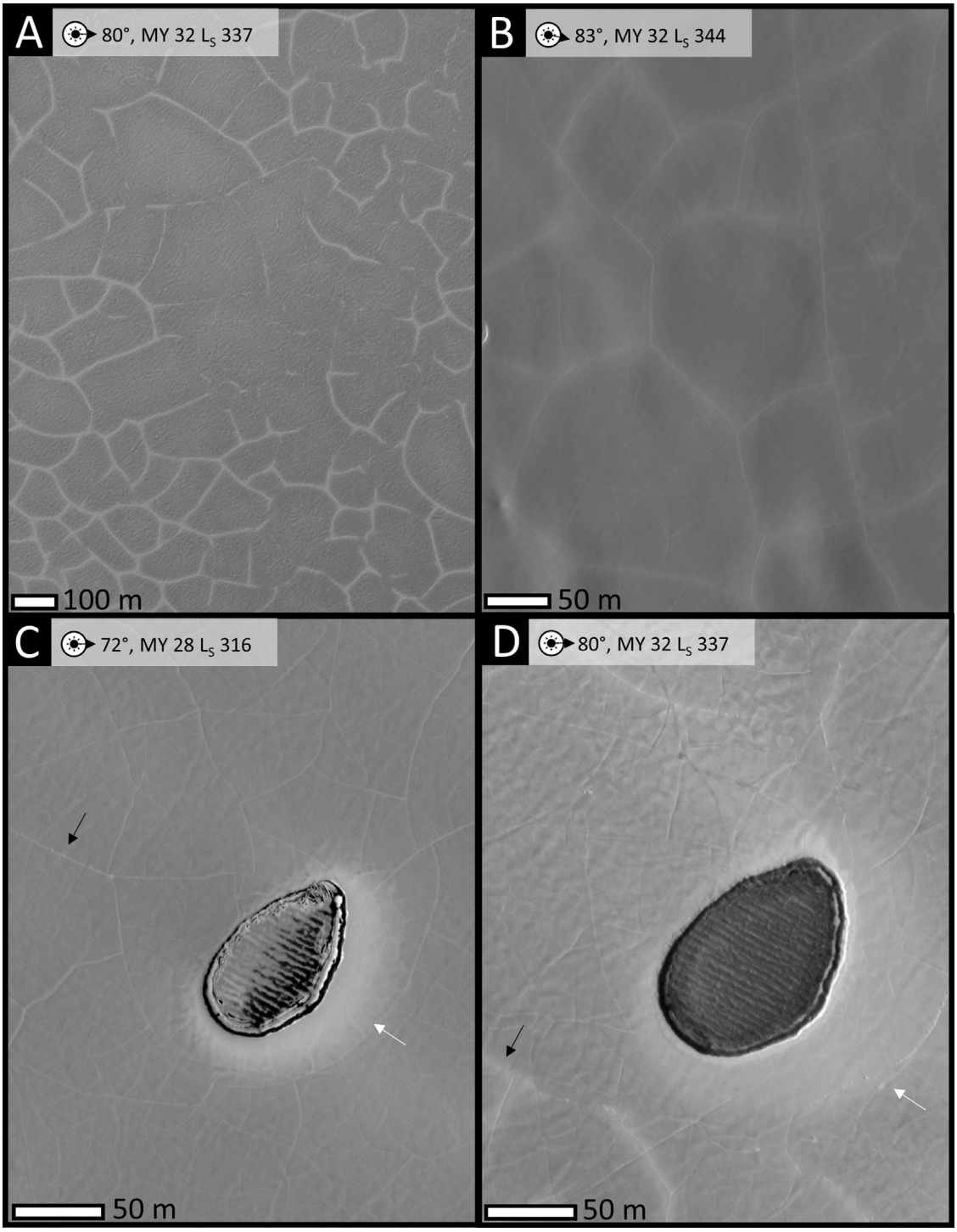

Fig. 12. a. Unit B2. b. The Un. In both locations new fractures have bright halos with widths of ~4–8 m. Note polygonal pattern of fracturing. c. Fractures are subtly bright after MY 28 dust storm (black arrow), and there are halos around steep scarps (white arrow). d. Halos around fractures and steep scarps after MY 32 dust cloud. HiRISE images (A) ESP_041107_0940 (B) ESP_041278_0930 (C) PSP_005359_0940 (D) ESP_041107_0940.

pressurization and venting occurs between the mesas of the RSPC, this venting would be invisible.

Finally, we observe more fans forming on the sides of RSPC mesas in MY 29 than in MY 28 or 31, which is similar to the variability in dark fan activity in the seasonal ice (Hansen et al., 2011). The variability in fan formation also correlates with the global dust storm in MY 28; however the correlation between enhanced fan activity and dust storms is not unambiguous (Hansen et al., 2011).

4.2. Interior sublimation drives fracturing and slab settling

The bright, upper surface layer of mesas undergoes brittle failure, fracturing and breaking into slabs (Figs. 9–12). We interpret this failure as resulting from the loss of underlying structural support as the interiors of mesas sublimate and lose mass (Fig. 26). As new fractures form across the CO_2 mesas, the upper surface breaks into progressively smaller slabs, until the slabs reach a surface area

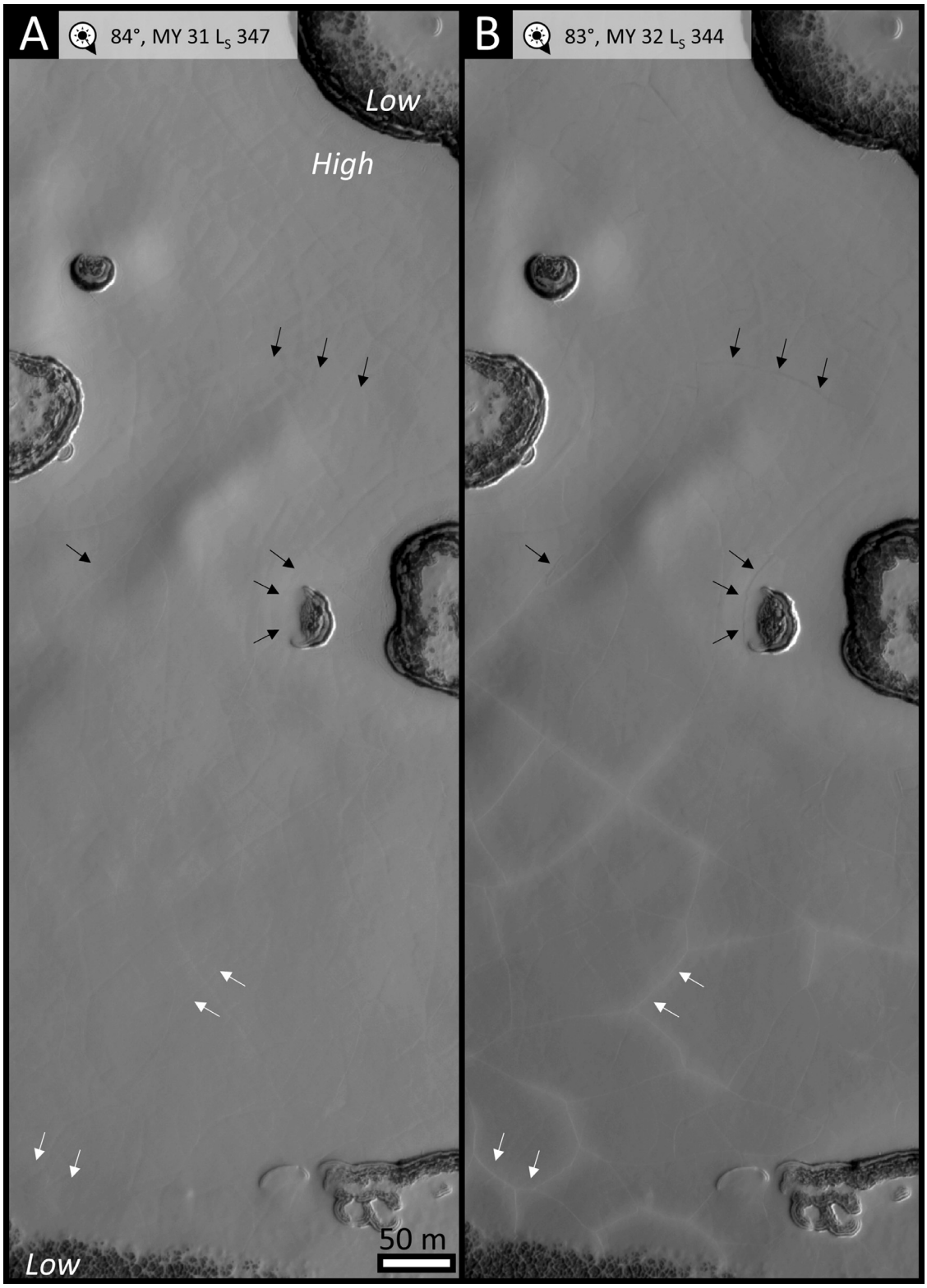

Fig. 13. a. The Un in late summer of MY 31. The CO_2 mesa is thinner toward the bottom of the image, where it smoothly drapes onto the H_2O ice basement, and thicker near the top of the image, where it terminates in a steep scarp. b. The same location one year later. New fractures with halos are apparent in the thinner part of the mesa (e.g. the features marked with white arrows), while new fractures without halos are apparent in the thicker part of the mesa (black arrows). HiRISE images (A) ESP_032535_0930, (B) ESP_041278_0930.

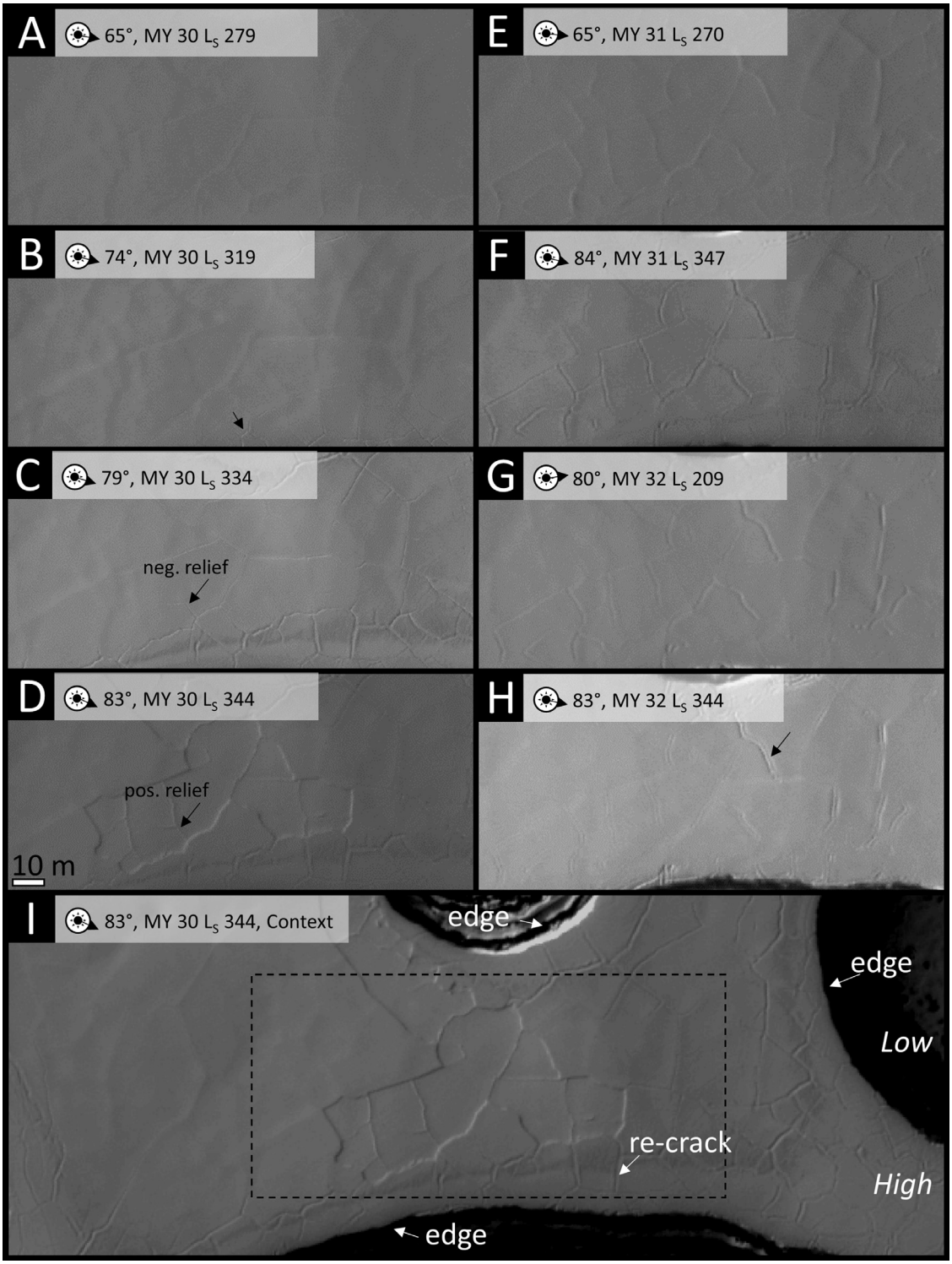

Fig. 14. a. Surface is generally smooth but some thin ridges are visible. b. Cracks form on some ridges (e.g. arrow). c. Cracking is more pronounced. d. A depression with an angular boundary appears. Note coincidence of boundary with ridges in panels A–C. e. Next year. Ridges are less crisp than in D, but more pronounced than in A. Note that the illumination geometry is similar to panel A. f. Cracks form on ridges. g. Next spring. Cracks are still apparent, but muted. h. Some cracks have a central ridge, forming a 'double crack' (e.g. arrow). i. Expanded view of D to give context for other panels. Note proximity to edge of mesa and re-cracking preferentially near mesa edges. HiRISE images (A) ESP_022210_0930 (B) ESP_023054_0930 (C) ESP_023410_0930 (D and I) ESP_023647_0930 (E) ESP_030834_0930 (F) ESP_032535_0930 (G) ESP_038403_0930 (H) ESP_041278_0930.

of $\sim 10^2$ m^2 (Figs. 14d and 16), which appears to be the scale on which slabs have enough strength not to break further. The natural result of internal sublimation and mass loss, fracturing, and collapse of mesas is the destruction of coherent layering, even if the CO_2 ice is originally deposited in layers. Others have also noted that it is impossible to find distinct layers within the RSPC deposits (e.g., Thomas et al., 2009).

The vermicular texture exposed in the interiors of mesas immediately after the erosion of the bright, upper surface indicates that sublimation and mass loss in the interiors of mesas is inho-

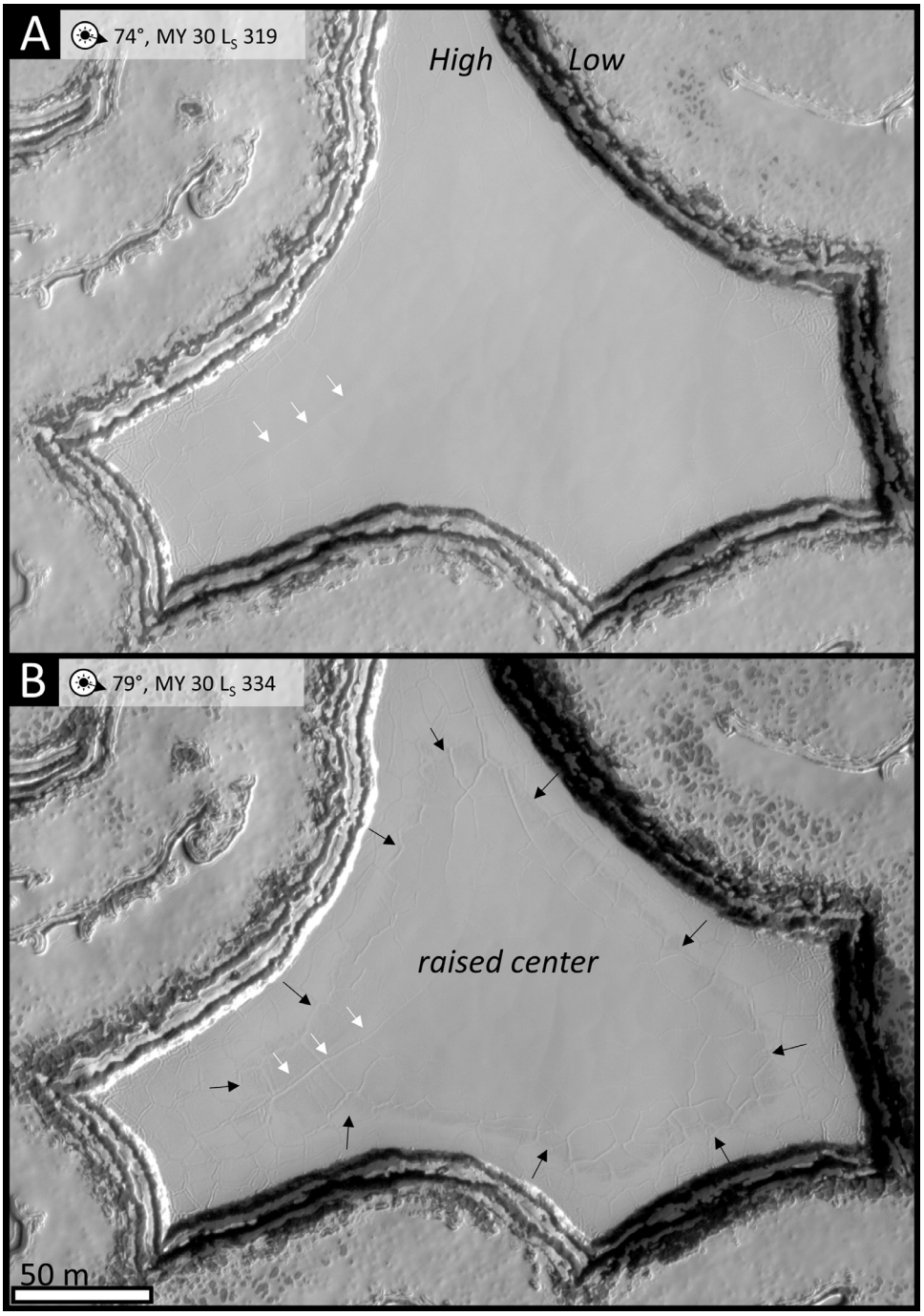

Fig. 15. The Un. a. Smooth upper surface of a mesa. b. 28 sols later, the mesa has a smooth, raised, lower albedo center and a lower, rougher perimeter. Black arrows indicate the approximate perimeter of the raised center. Also note re-cracking (white arrows). HiRISE images (A) ESP_023054_0930, (B) ESP_023410_0930.

mogeneous (see Figs. 17 and 5d of Thomas et al. (2005)). The vermicular texture may be the result of channels formed by the lateral flow of pressurized gas (cf. Kieffer, 2003, 2007; Kieffer et al., 2006; de Villiers et al., 2012). Non-uniform structural support from the uneven, vermicular texture directly underlying the bright, upper surface may be the reason that slabs tilt during collapse.

The vertical offset in the fractures between adjacent slabs is initially crisp, but becomes muted by the time observations are made the following spring (Fig. 11). Since fractures only become muted during the winter, the muting is likely due to the deposition of new CO_2 ice (Fig. 26). After becoming muted, some fractures become double-ridged and, in one instance, a new subtle ridge simultaneously appears ~10 m away and parallel to the original fracture (Fig. 11). We therefore interpret that double ridges occur when slabs undergo additional settling. Fractures also sometimes re-crack (Figs. 14c, f and 16d), which we interpret as evidence of additional settling of slabs exploiting preexisting fracture boundaries. Re-cracking occurs preferentially within a few tens of meters of mesa edges that are bounded by ~1–10 m-tall sheer scarps (Figs. 14i and 16d), and some mesas bound by tall, sheer scarps have raised centers (Fig. 15). These observations indicate that internal sublimation and mass loss is enhanced close to mesa sides, leading to increased subsidence, likely due to sunlight efficiently

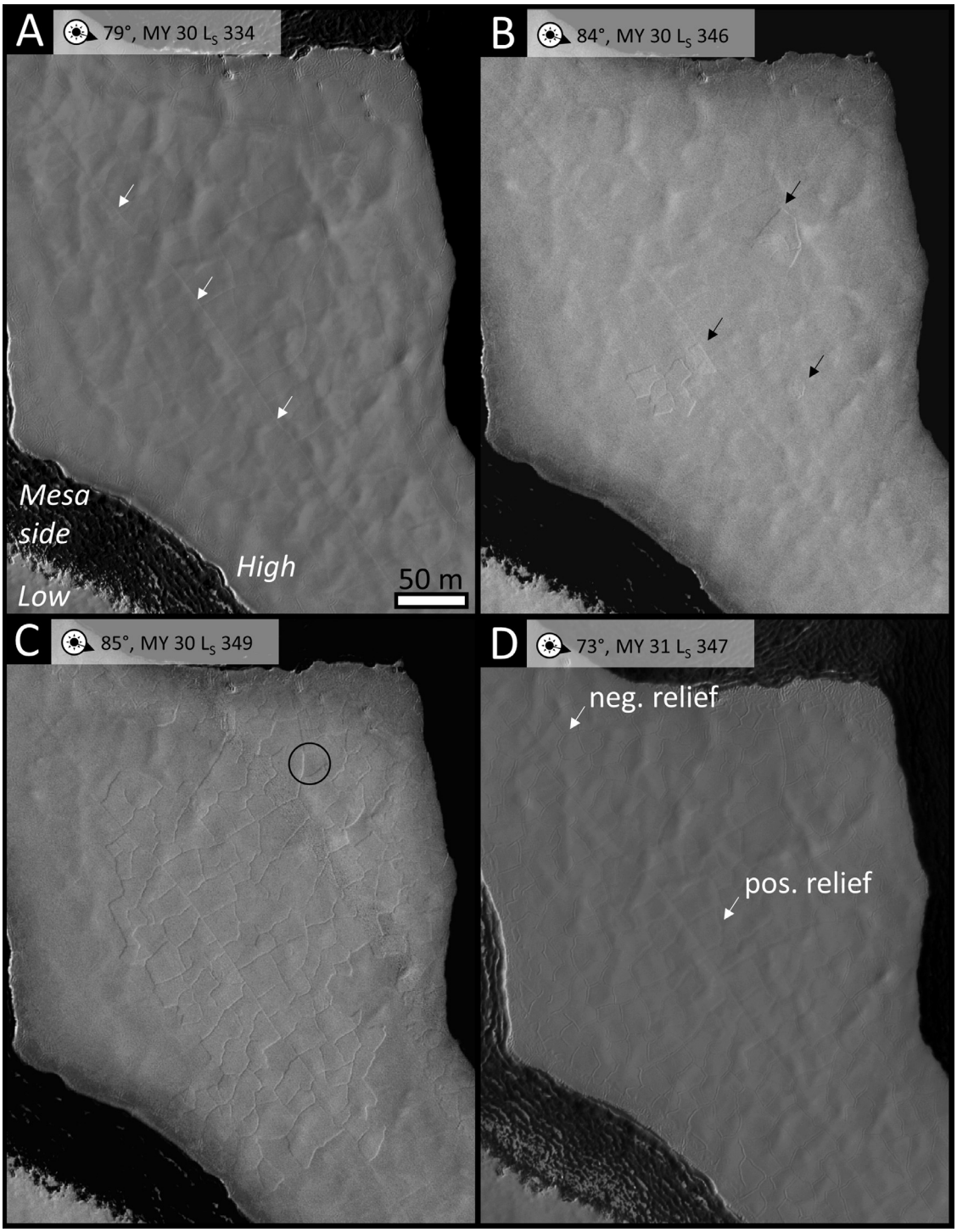

Fig. 16. Unit A0. Time series spanning 29 sols. a. Note long ridge. b. Polygonal depressions appear. c. 6 sols later. Nearly entire upper surface is covered in polygonal depressions. Note some polygonal shapes are still in positive relief (e.g. circled). d. One martian year later. Note positive relief of ridges further than ~40 m from the mesa edge and negative relief of ridges within ~40 m of the edge. HiRISE images (A) ESP_023410_0930, (B) ESP_023700_0930, (C) ESP_023779_0930, (D) ESP_032535_0930.

penetrating horizontally into the mesas because the sun is low on the horizon near the pole.

Fractures with negative relief sometimes become positive relief ridges that later return to negative relief (Fig. 14c-f), and some fractures that have re-cracked develop a ridge within the fracture (Fig. 14h). We interpret these observations as the infilling of fractures between slabs with new CO_2 ice, forming a wedge that vertically settles independently of the adjacent slabs. We interpret the bright, ~1-m-wide ridges left behind between slabs as the upper surface deteriorates (Fig. 17) as the remnants of these wedges.

Finally, the occurrence of fields of polygonal depressions in at least one location each year indicates that the formation of polygonal depressions is a common process. However, the timing between widespread subsidence events at a particular location appears to be longer than our five-martian-year observational baseline, because we do not observe these subsidence events more than once in any specific location. Nevertheless, the nearly ubiq-

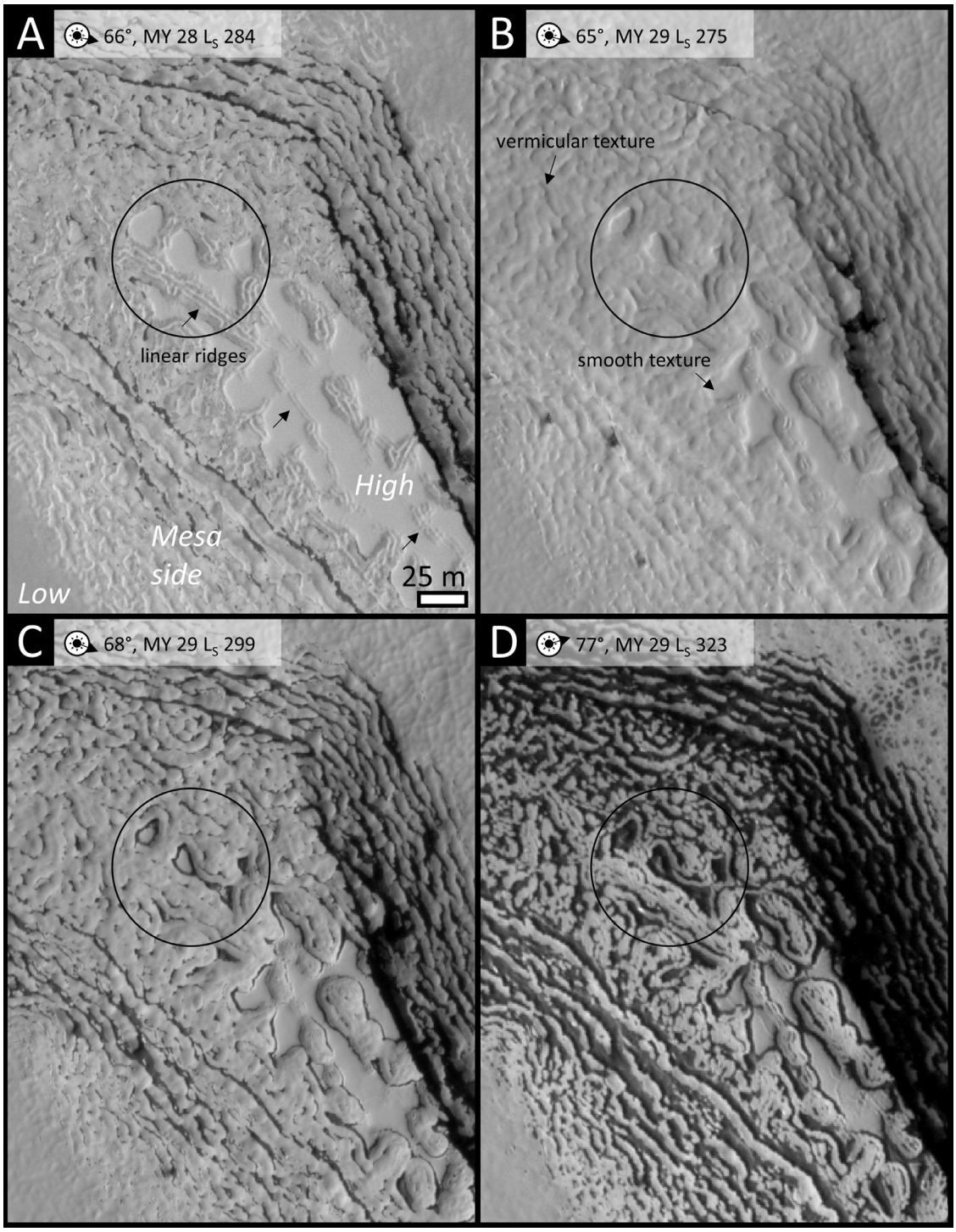

Fig. 17. Unit A0. a. Vermicular texture of mesa interior apparent under smooth, upper surface. Note linear ridges between broader smooth patches. b. ~1 martian year later. Smooth patches are smaller. c. Note change of albedo as upper surface deteriorates. d. Upper surface and sides of mesa are becoming dark. HiRISE images (A) PSP_004686_0930, (B) ESP_013309_0930, (C) ESP_013810_0930, (D) ESP_014339_0930.

uitous development of polygonal depressions on Unit A0, where there is HiRISE coverage during MY 30, indicates ~1% of local mass loss from the interior, since polygonal depressions settle downwards by ~10 cm and the A0 mesas are ~10 m thick (Thomas et al., 2016). If the entirety of Unit A0 underwent this subsidence, then $\sim 3 \times 10^7$ m^3 of CO_2 would be lost (on the order of 0.01% of the mass of the entire RSPC). Continued observations of polygonal slab settling are warranted because, once a settling frequency can be established, the rate of interior sublimation can be calculated. For now, we estimate an upper bound of 2 cm/martian year of internal sublimation loss in Unit A0 (10 cm of settling over 5 martian years).

4.3. Interior sublimation rates based on halos around fractures

Bright halos that developed around new fractures in MY 32 (Fig. 12) may signal gas venting from fractures on the upper surface of the mesas. The bright halos occurred after a large dust

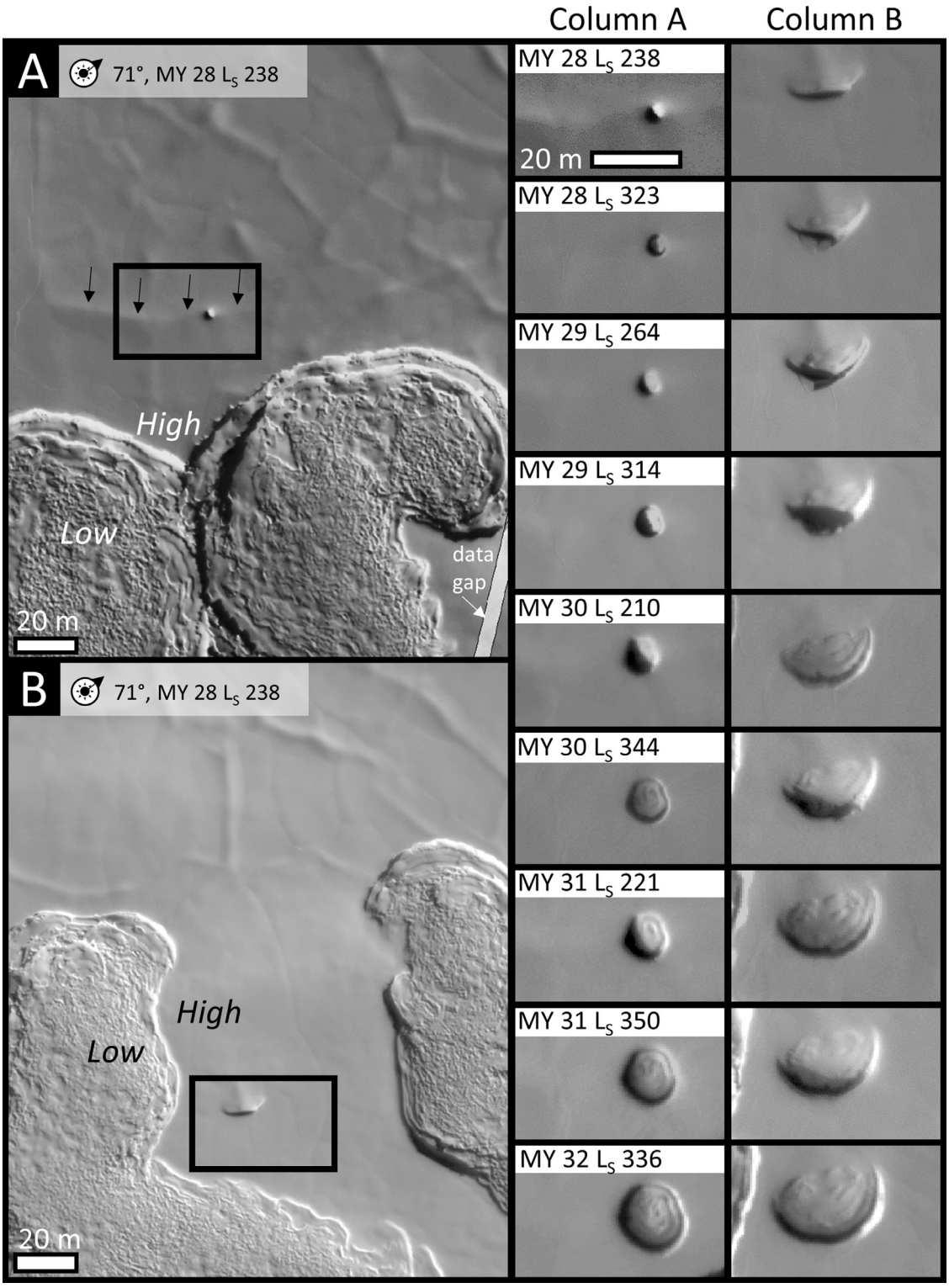

Fig. 18. Unit A1. a. Context for Column A. Note pit forming along crack (arrows). b. Context for Column B. Columns A and B are a time series of two nascent pits from mid-spring of MY 28 to late summer of MY 32. The context images are the same as the first image in each time series. Note the pit in Column A has a flat floor, while the pit in Column B has a slanted floor that smoothly connects to the upper surface of the mesa along the upper margin. HiRISE images PSP_003738_0930, PSP_005517_0930, ESP_013086_0930, ESP_014141_0930, ESP_020800_0930, ESP_023661_0930, ESP_029846_0930, ESP_032615_0930, ESP_038483_0930, ESP_041094_0930.

cloud was present over the south polar cap from ~L_S 310–320 in MY 32,[1] suggesting a connection between the halos and the dust cloud. Becerra et al. (2014) also note bright halos on mesa edges following a dust storm in MY 28 and develop a conceptual model for their formation in which pressure from sublimating gas on the sides of mesas deflects falling dust, such that, while other regions of the RSPC darken from dust deposition, the mesa edges are protected and remain bright. Becerra et al. (2014) also consider two alternatives of halo formation by either (i) inclusion of H_2O ice im-

[1] MRO MARCI weather reports on 03/25/2015 and 04/15/2015 from Malin Space Science Systems.

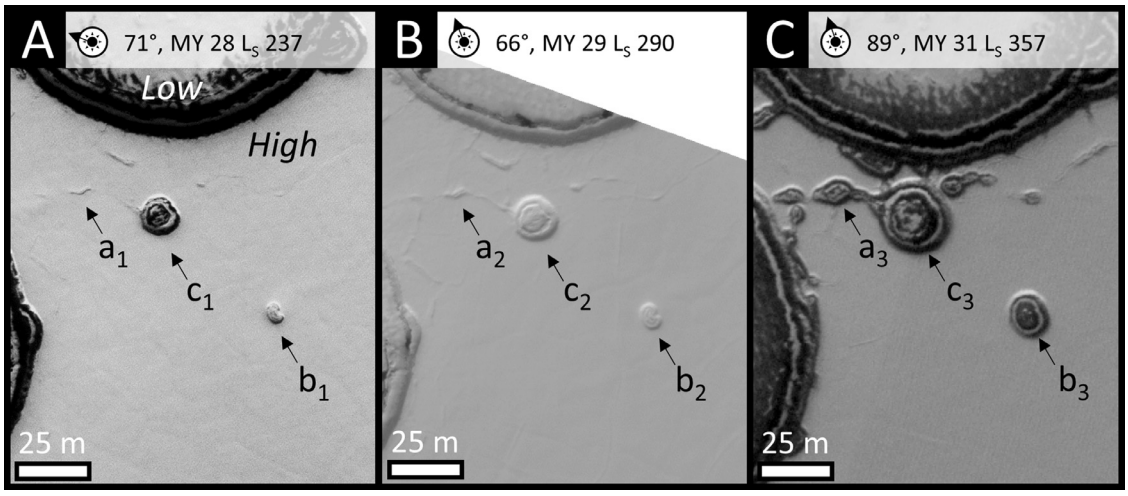

Fig. 19. Unit B7. a. Cracks on the top surface of the CO_2 deposit. b. 1 martian year later. c. Another 2 martian years later. The evolution of a fracture widening into a quasi-circular pit can be tracked by observing changes from a_1 to c_3 in sequential order: a_1 is a fracture that evolves to a_3; a_3 and b_1 have similar size and morphology; b_1 evolves to b_3; b_3 and c_1 have similar size and morphology; c_1 evolves to c_3, a quasi-circular pit. HiRISE images (A) PSP_003716_0930, (B) ESP_013617_0930, (C) ESP_032790_0930.

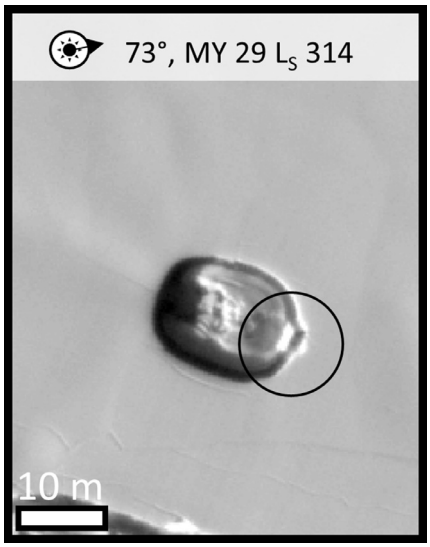

Fig. 20. Unit A1. The smallest pit observed to erode via calving blocks. Calving block is about 1 × 3 m and is circled. HiRISE image ESP_014141_0930.

purities or (ii) the deposition of fine-grained CO_2 frost, but reject both alternatives based on spectral data. Our data are consistent with Becerra's interpretation of sublimation, and we find that halos occur almost exclusively around new fractures that were not visible in previous years, which likely indicates that most older fractures become sealed, thus stopping gas outflow.

Under the interpretation that the halos are caused by CO_2 outflow deflecting dust, the halos provide an opportunity to estimate the sublimation rates within the mesas. Dust will be deflected when the velocity of the venting gas approximately equals the velocity of the settling dust (v_s). Dust falls in the Stokes regime (Becerra et al., 2014), so v_s can be found with:

$$v_s = \frac{1}{18}\frac{(\sigma - \rho)d^2 g}{\eta} \quad (1)$$

Here we adopt the same values as Becerra et al. (2014): ρ is the atmospheric density (~0.02 kg m^{-3}), σ is the density of the dust particle (~2700 kg m^{-3}), g is martian gravity (3.7 m s^{-2}), and η is the atmospheric viscosity (~1.3×10^{-5} Pa s). We use a particle diameter of 2 μm (d, Wolff and Clancy, 2003; Wolff et al., 2009).

The gas velocity (v_g) at a distance r from the fracture depends on mass flux per unit length ($\dot{m}$) and is given by:

$$v_g = \frac{\dot{m}}{\pi r \rho} \quad (2)$$

We can now calculate the total CO_2 gas flux through the linear fractures for the areas shown in Fig. 12a and b. The average lateral extent of the halos in both locations in MY 32 is $r \sim 3$ m, so rearranging Eq. (1) and (2) and solving for $\dot{m}$, the flux of CO_2 gas from the vents is 3×10^{-5} kg m^{-1} s^{-1}. The total length of fractures in Fig. 12a (Unit B2) is 1.6×10^4 m, so the total flux through the vents is 0.5 kg s^{-1}. Assuming a local source area for the sublimating gas, i.e., the area of Fig. 12a (1.7×10^6 m^2), the internal sublimation rate is 3×10^{-7} kg m^{-2} s^{-1}. The total length of fractures in Fig. 12b (the Un) is 2.2×10^3 m, and the total area is 1.3×10^5 m^2, yielding a similar internal sublimation rate of 5×10^{-7} kg m^{-2} s^{-1}. We note that our estimate of mass flux is lower than the one modeled by Becerra et al., (2014), which makes sense since they modeled the outflow from the sublimation of the surface of the pit walls, where the halos are also observed to be larger.

Assuming a mean density of 1500 kg m^{-3} for CO_2 ice (see Aharonson et al., 2004; Blackburn et al., 2010; Smith and Zuber, 2011, Hayne et al., 2012, 2014; Thomas et al., 2016), and assuming an average thickness of ~1 m for the deposits displaying fractures with halos (Section 3.2), the area of B2 shown in Fig. 12a loses 2.0×10^{-10} of its total mass each second and the area of the Un shown in Fig. 12b loses 3.6×10^{-10} of its total mass each second. If these rates continue through the entire spring and summer season, then ~0.6% of the mass (a thickness of ~0.6 cm) from the B2 area (Fig. 12a) and ~1.1% of the mass (a thickness of ~1.1 cm) from the Un area (Fig. 12b) is lost to internal sublimation. These rates are about half the upper bound placed on sublimation in the thicker mesas based on slab settling.

It is interesting that the thicker mesas do not have halos around new fractures. The phenomenon is likely real, since thicker mesas with new fractures are within the HiRISE image of the Un. This may be due to the fact that thicker mesas are typically surrounded by tall, steep scarps, whereas the boundaries of the thinner mesas are typically thin, smooth ramps. We hypothesize that gas can therefore more easily escape through the sides of thick mesas, leading to decreased flux through their tops, and thus inhibiting halo formation.

Finally, we extend two caveats. First, the vertical settling speed of dust is ~2×10^{-4} m s^{-1} (Eq. (1)), while Smith et al. (2015) model

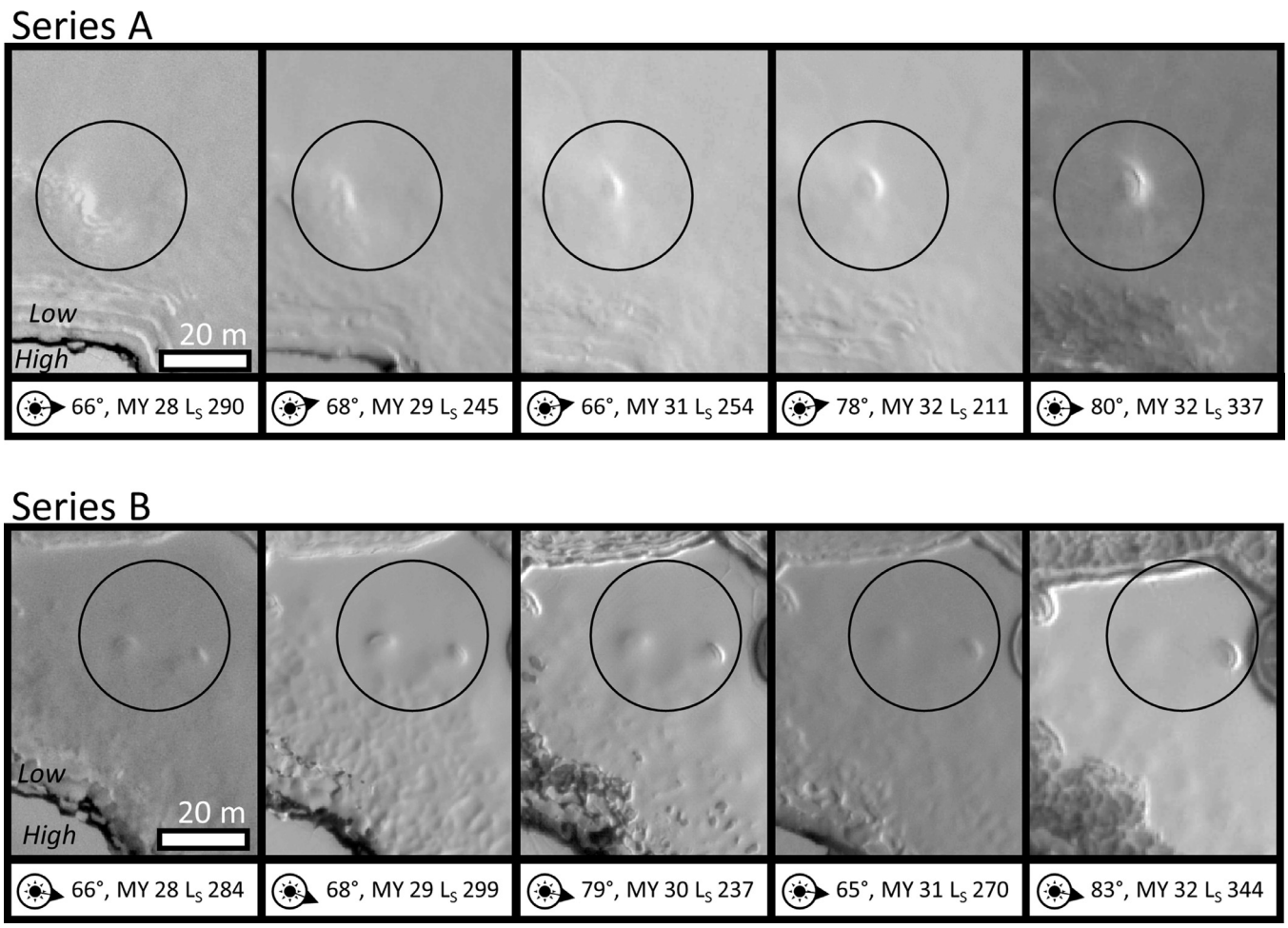

Fig. 21. Unit B2. 5-martian-year time series. a. The edge of a thin CO_2 deposit. Note roughness on the edge of the deposit in the first image. A crescent is clearly recognizable in the final image. b. Two crescents are apparent in the first image. Left crescent is muted, but still apparent in third image. Only one crescent is apparent in the final image. Note low illumination angle. HiRISE images (A) PSP_004792_0940, ESP_012690_0940, ESP_030518_0940, ESP_038443_0940, ESP_041107_0940 (B) PSP_004686_0930, ESP_013810_0930, ESP_023410_0930, ESP_030834_0930, ESP_041278_0930.

the ambient wind speed at a height of 20 m above the RSPC to be on the order of several meters per second or greater. Even though wind speeds are well-known to decrease quickly approaching the atmosphere-ground interface, ambient wind may still strongly effect the ability of pressurized gas from sublimating CO_2 to deflect dust grains. Second, while observations of Unit B2 following the dust storm in MY 28 show that fractures are brighter than the surrounding areas, the lateral extent of the brightening is only ~0.75 m on either side of the fracture, suggesting that the sublimation rate in the MY 28 observations is only one-fourth that of the observations in MY 32; the halos around the mesa edges are also less extensive in MY 28 than in MY 32 (Fig. 14c-d). This may indicate (i) decreased interior sublimation after the larger and longer-lived MY 28 dust storm, perhaps because more sunlight was blocked during summer, (ii) intra- or inter-annual variation in internal sublimation rates, or (iii) a difference in halo degradation due to post-dust storm surface changes, caused by a difference in seasonality (and thus insolation) or amount of dust deposition (and thus albedo).

4.4. Seasonal CO_2 ice incorporated into the RSPC

The development of smooth ramps, which is necessary for the development of linear troughs and moats, requires vertical accumulation (Section 3.4 and 3.5), and thus indicates the importance of deposition in determining the morphology of the RSPC. Additionally, the striking change in relative albedo of mesa sides and the H_2O ice basement adjacent to RSPC mesas compared to the tops of mesas over the course of spring and summer (e.g. compare Fig. 6a and b) clearly indicates the deposition of seasonal CO_2 ice on both mesa sides and the H_2O ice basement. Given the scale and proximity of this deposition to mesa tops, significant amounts of CO_2 are likely also deposited on the upper surface of the mesas.

Thomas et al. (2016) also report growth of smooth mesa edges over three martian years (between MY 28 and 30) in Unit A2 (their Fig. 4); although, due to limited HiRISE coverage of Unit A2, their observations in MY 30 (L_S 309) are at an earlier time in the summer than their observations in MY 28 (L_S 323). This leaves open the possibility that the increased extent of the gentle scarp could be due to the presence of seasonal CO_2 ice that will sublimate later in the summer. However, the progressive muting of fractures (Fig. 11) and progressive growth along mesa edges (Fig. 25) observed in our multi-year data indicates that at least some of the seasonal deposition is permanently incorporated into the RSPC on annual timescales, particularly since the extent of the gentle scarps in Fig. 25 is greater later into the summer in two successive Mars years. Moreover, we observe widespread fracturing and settling of the upper surface, with an enhanced rate of settling near steep mesa edges, whereas Thomas et al. (2016) made shadow measure-

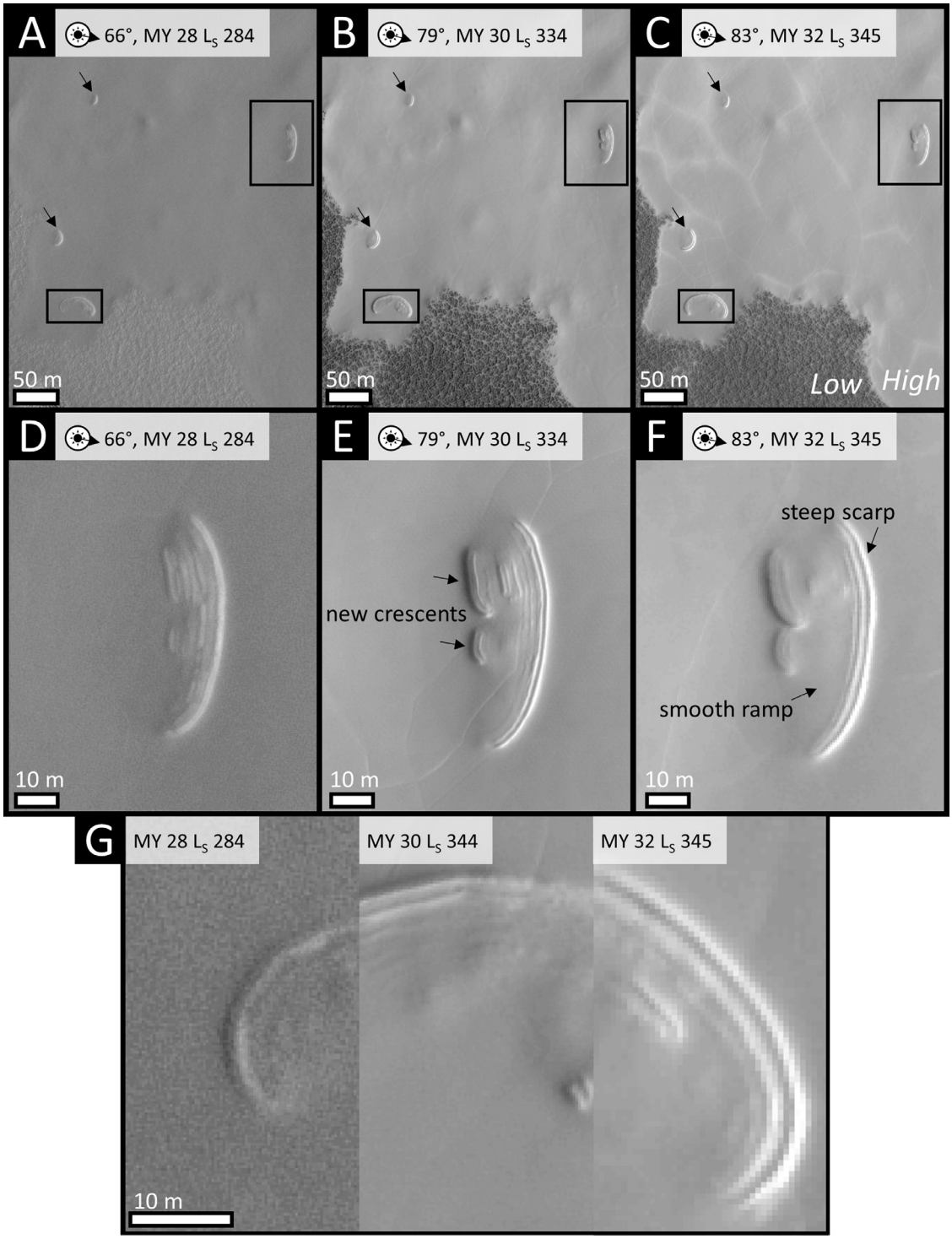

Fig. 22. The Un. a–c. Time series of crescents. Arrows are georeferenced and mark fixed locations between the images. Note positions of small crescents change relative to the arrows. Black boxes indicate the locations of panels d–g. Lower panels are insets of upper panels (black boxes). d. Zoom in on crescent. e. Note that two new crescents have formed from roughness on the gentle slope. f. The new crescents and the original scarp have eroded away from each other. g. Georeferenced slices of a crescent in three different years. Note that the smooth ramp still abuts the steep scarp in the rightmost slice, despite the fact that the steep scarp has eroded. HiRISE images PSP_004686_0930, ESP_023410_0930, ESP_041278_0930.

ments indicating that there has been almost no change in mesa thickness over periods of 3–22 martian years (depending on coverage). Therefore, the rates of subsidence of the upper surface of mesas and net deposition onto the upper surface of mesas seem to be nearly balanced on annual to decadal timescales.

4.5. Scarp steepness and the deposition-sublimation cycle as landform drivers

Fractures and smooth ridges that have vertical offsets of $<$ ~10 cm and lengths of tens to hundreds of meters do not, once formed, retreat backward in subsequent years (Fig. 11). Addition-

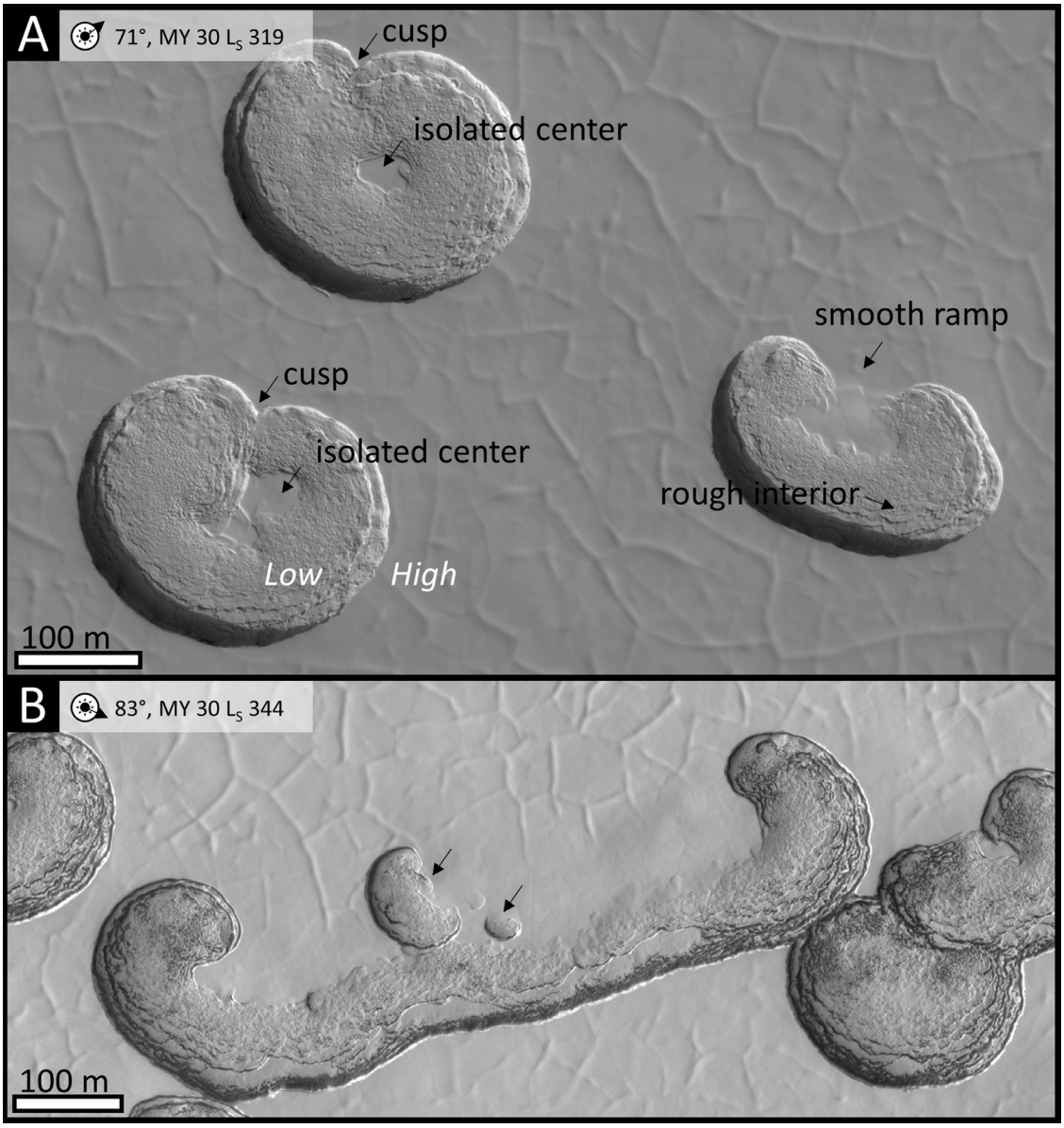

Fig. 23. a. Heart-shaped pits can exhibit smooth ramps and smooth, isolated centers. Note encroachment of steep scarp on smooth ramp. b. Half-circle pits can also form elongated troughs with curled ends in which the length of the ramp is greater than the width of the pit. Note forms intermediate between half-circle pits (Fig. 18b) and heart-shaped pits in panel a (arrows). HiRISE images (A) PSP_003738_0930, (B) ESP_023661_0930.

ally, smoothed pit-shaped depressions are stable morphologies in all locations we observe, despite having vertical relief on the order of tens of centimeters (Figs. 6 and 21b). However, rough alcoves that are ~5 m long and have ~10 s of centimeters of relief develop into crescentic pits (Fig. 21a), and steep-walled pits with ~2 m radii and ~10 cm of relief will enlarge (Fig. 18). Thus, ~10 cm of steep vertical offset along a curved extent of a few meters is the threshold for a steep scarp that will continue to erode in subsequent years despite winter deposition. The two crescents in Fig. 21b illustrate this threshold. Each initially has a vertical scarp with ~10 cm relief (based on shadow measurements, with an uncertainty of ~3 cm) and a curved extent of a few meters, but the left pit is smoothed over, while the right pit maintains a steep scarp.

Scarp steepness, curvature, and albedo play an important role in the development of pits (Fig. 27). Scarps will absorb, reflect, and reemit sunlight. Steeper scarps expose the dustier, darker interior of mesas and therefore absorb more energy than smooth ramps, which are protected by the bright capping layer of cleaner ice (Section. 4.1; Fig. 24). In addition, steep scarps reflect and re-emit more energy back into a pit than a shallow ramp (Fig. 27a). Curved scarps will also reflect and reemit energy onto neighboring sections of the scarp, whereas a linear scarp will reflect energy away (Fig. 27a). Surface roughness in general will focus energy, such as in the development of quasi-circular pits from points of collapse or fracture widening (Fig. 27a). We note that the landscape evolution model of Byrne et al. (2008, 2015) predicts that pits will form once a critically steep slope is developed, which supports this theory. However, the Byrne et al. (2008, 2015) model achieves steep slopes via differential accumulation of CO_2 ice, whereas we prefer a framework in which steep, sublimating slopes form from the fracturing and collapse of the upper surface of mesas, because we only observe pit formation in intimate association with fractures (e.g. Fig. 18).

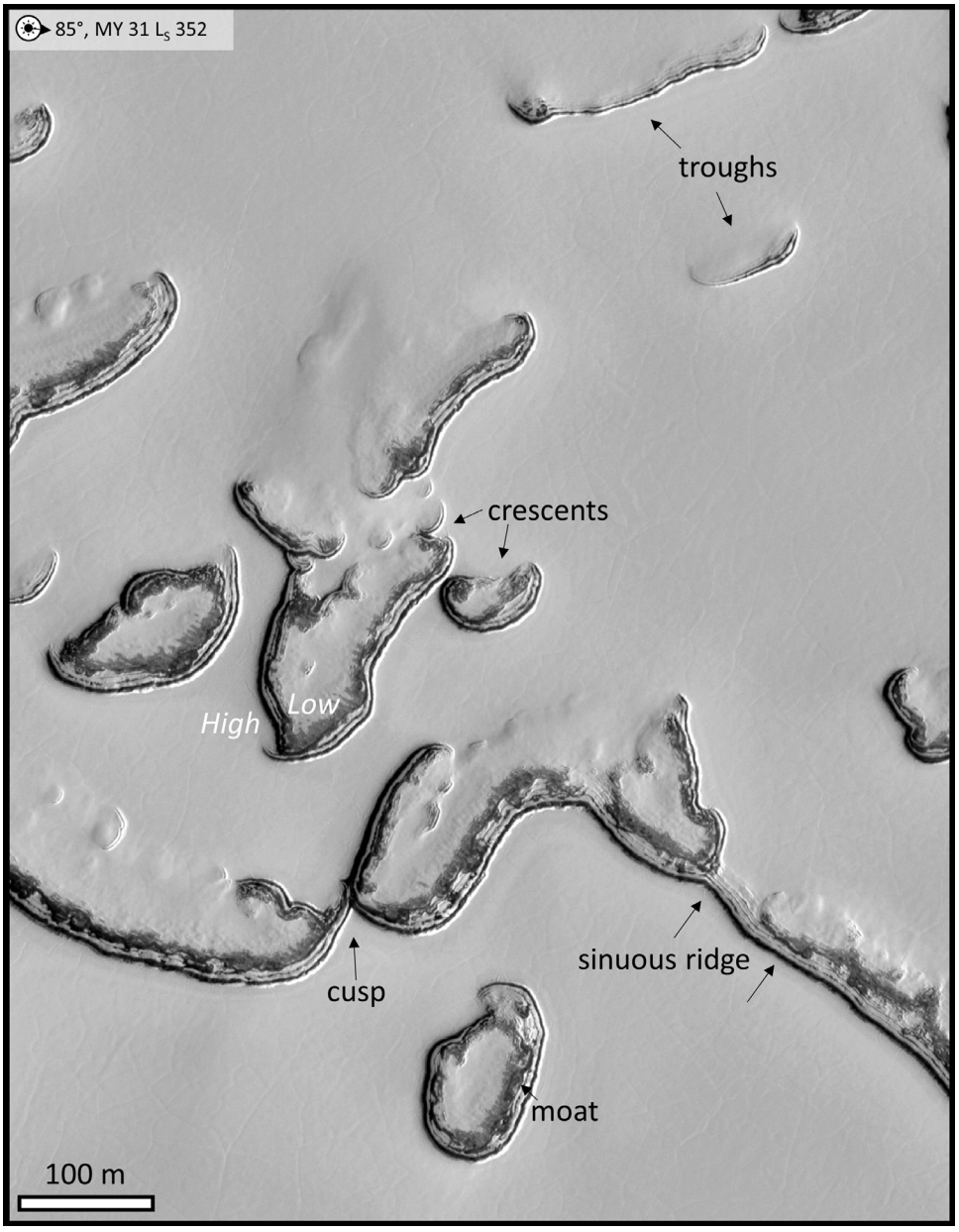

Fig. 24. Unit B2. Crescents, linear troughs, sinuous ridges, and moats. Note cusps where ridges intersect. HiRISE image ESP_032654_0940.

The balance of deposition and erosion at the boundary between the steep scarp and the smooth ramp in half-circle pits (Fig. 18b) drives its evolution either toward a linear trough or a heart-shaped pit (Section 3.5; Fig. 27b and c). If deposition along the ramp approximately keeps pace with erosion along the opposing scarp face, the distance between the ramp and the opposing steep scarp face remains approximately constant; however, the increased curvature at the edges of the pits focuses reflected energy (Fig. 27biii), causing increased erosion and lengthening the pit, which creates a linear trough (Fig. 27b). On the other hand, if scarp erosion definitively outpaces deposition on the smooth ramp, the pit widens and lengthens approximately symmetrically. The most strongly curved portion of the pit erodes most rapidly (Fig. 27cii), cuts into the ramp, and eventually dissects it, forming a cusp and making a heart-shaped pit (Fig. 27c).

The spatial variation of morphologies in the RSPC indicates that differences in insolation, deposition rates (e.g. Brown et al., 2014), composition, or winds (e.g. Smith et al., 2015) across the RSPC may lead to greatly different outcomes in morphology. Additional observation and modeling of the RSPC is warranted in order to uncover which of these parameters are most important in developing the final morphology of a particular unit.

5. Conclusion

We use high-resolution, high-cadence time series observations of the martian residual south polar cap (RSPC) to understand its morphologic evolution at the meter-scale. We document, for the first time, dark fans on the sides of mesas, and fracturing and collapse of the upper surface of mesas. We interpret that the dark fans result from pressurized gas escape from the sides of mesas carrying entrained dust, and indicate sublimation of CO_2 ice in the interior of RSPC mesas. Our analysis indicates that sublimation within mesas is mediated by mesa thickness as well as by verti-

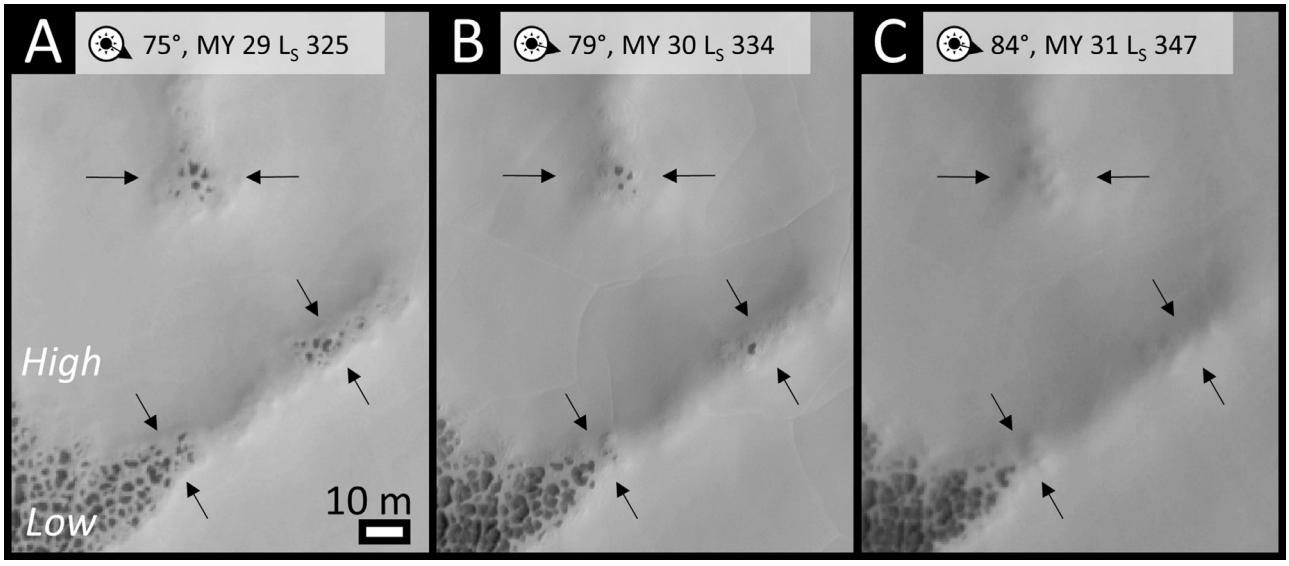

Fig. 25. a, b, c. The Un. Time series of the smooth edge of a CO_2 mesa over three martian years, with each successive image taken later in the summer. Smooth, bright texture is CO_2 ice. Dark, rough texture is H_2O ice. Note growth of CO_2 ice (arrows). Note roughness in panel B. d. Context. Note distance between gentle scarp and nearest steep scarp. HiRISE images (A,D) ESP_014390_0930, (B) ESP_023410_0930, (C) ESP_032535_0930.

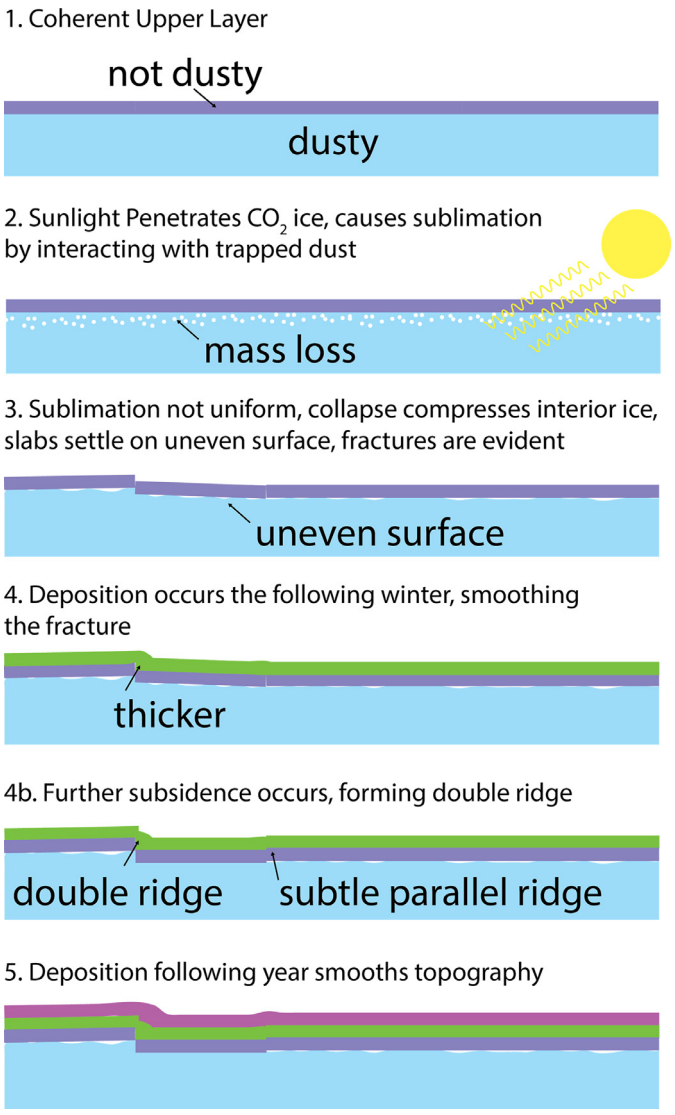

Fig. 26. Interpretation of the development of fractures. Compare to Fig. 11. Note that development of double ridge is not ubiquitous among fractures.

cally stratified dust content. Under this scenario, the sublimation leads to mass loss and therefore loss of structural support for the brittle upper layer of the mesas, which fractures into collapsing polygonal slabs. Thin (~1 m) mesas have an internal sublimation rate of 6×10^{-6} to 1×10^{-5} kg m^{-2} s^{-1} of CO_2, leading to gas escape through fractures that is sufficient to prevent localized dust deposition, while thick (several meter) mesas appear to have sublimation rates that are 5–10 times lower.

We find that the collapse of mesa tops creates slabs separated by fractures. Small areas of collapse along the fractures and fractures that appear to settle and re-crack evolve into steep-walled, quasi-circular pits. The steep walls act to focus sunlight, enhancing erosion and preventing winter deposition from smoothing them back over. We infer that steep scarps need to have at least ~10 cm of sheer vertical relief, lengths of ~>5 m, and curvature in order for summer erosion of the scarps to outpace smoothing over by wintertime deposition.

Our analysis indicates that localized collapse along pre-existing fractures where a portion of the collapsing material remains attached to the upper surface leads to crescentic pits, which are pits that have smooth ramps that abut steep scarps. Uneven deposition along the edges of smooth ramps can create steep-scarped alcoves that can also develop into crescentic pits. We interpret that the relative effectiveness of deposition and erosion at the boundary between the smooth ramp and the steep scarp determines whether a crescentic pit develops into a heart-shaped pit or a linear trough.

The processes we infer from our observations are capable of explaining the morphologies present in the RSPC and provide a framework for landscape evolution models that would lead to better insight into the material properties of the RSPC. Ultimately, the processes we describe in this paper shed light on the subtle interplay of deposition and erosion on the RSPC and inform our understanding of the global martian CO_2 cycle.

Acknowledgments

We gratefully acknowledge funding from NESSF grant #16-PLANET16F-0071 and MFRP grant #NNX14AG54G. We also thank Timothy Titus and an anonymous reviewer for their feedback, which helped to improve this work.

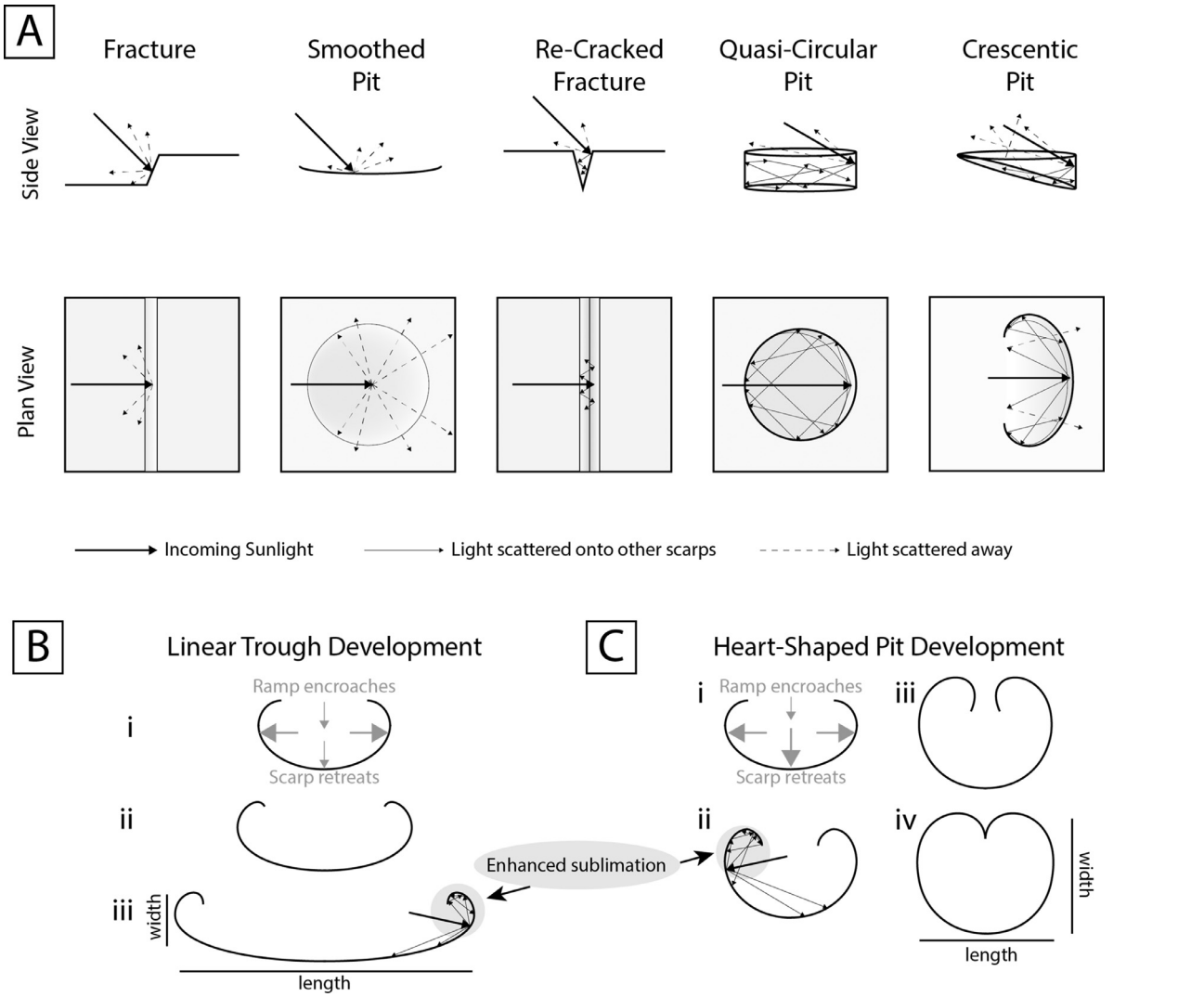

Fig. 27. a. Light scattering geometries in the RSPC. Light is scattered away from fracture scarps and smoothed pits (e.g. Fig. 6). Sunlight is scattered into and absorbed by the steep scarps in meter-wide re-cracked fractures and quasi-circular pits. The low-angle, smooth ramp in crescentic pits reflects light away, but the steep-scarped, curled ends efficiently trap light. b. The smooth ramp in crescentic pits lengthens and the scarp retreats lengthwise, while the ramp extends into the pit, approximately maintaining the same distance between the ramp and the opposite scarp from year to year. This creates a linear trough. c. The scarp retreat cuts into the smooth ramp, until the scarps meet in a cusp, creating a heart-shaped pit. Retreat of the scarp opposite the ramp also outpaces growth of the ramp into the pit, widening the pit.

References

Aharonson, O., Zuber, M.T., Smith, D.E., Neumann, G.A., Feldman, W.C., Prettyman, T.H., 2004. Depth, distribution, and density of CO2 deposition on Mars. J. Geophys. Res. E Planets 109, 1–10. doi:10.1029/2003JE002223.

Becerra, P., Byrne, S., Brown, A.J., 2014. Transient bright "halos" on the south polar residual cap of Mars: implications for mass-balance. Icarus 251, 211–225. http://doi.org/10.1016/j.icarus.2014.04.050.

Bierson, C.J., Phillips, R.J., Smith, I.B., Wood, S.E., Putzig, N.E., Nunes, D., Byrne, S., 2016. Stratigraphy and evolution of the buried CO_2 deposit in the Martian south polar cap. Geophys. Res. Lett. 43, 1–8. (May) http://doi.org/10.1002/2016GL068457.

Blackburn, D.G., Bryson, K.L., Chevrier, V.F., Roe, L.A., White, K.F., 2010. Sublimation kinetics of CO_2 ice on Mars. Planet. Space Sci. 58, 780–791. doi:10.1016/j.pss.2009.12.004.

Brown, A.J., Piqueux, S., Titus, T.N., 2014. Interannual observations and quantification of summertime H_2O ice deposition on the Martian CO_2 ice south polar cap. Earth Planet. Sci. Lett. 406, 102–109. doi:10.1016/j.epsl.2014.08.039.

Byrne, S., Hayne, P.O., Becerra, P., 2015. Evolution and stability of the residual CO_2 ice cap. In: Proceedings of the 46th Conference on Lunar and Planetary Science #1657.

Byrne, S., Ingersoll, A.P., 2003. A sublimation model for Martian south polar ice features. Science 299 (5609), 1051–1053. http://doi.org/10.1126/science.1080148.

Byrne, S., Russell, P.S., Fishbaugh, K.E., Hansen, C.J., Herkenhoff, K.E., McEwen, A.S., Team, Hirise, 2008. Explaining the persistence of the southern residual cap of Mars: HiRISE data and landscape evolution models. In: Proceedings of the 39th Conference on Lunar and Planetary Science, pp. 10–11. Retrieved from http://adsabs.harvard.edu/abs/2008LPI....39.2252B.

de Villiers, S., Nermoen, A., Jamtveit, B., Mathiesen, J., Meakin, P., Werner, S.C., 2012. Formation of Martian araneiforms by gas-driven erosion of granular material. Geophys. Res. Lett. 39 (13), 1–5. http://doi.org/10.1029/2012GL052226.

Durham, W.B., Kirby, S.H., Stern, L.A., 1999. Steady-state flow of solid CO_2: preliminary results. Geophys. Res. Lett. doi:10.1029/1999GL008373.

Eluszkiewicz, J., 1993. On the microphysical state of the Martian seasonal caps. Icarus (103) 43–48.

Guo, X., Lawson, G.W., Richardson, M.I., Toigo, A., 2009. Fitting the Viking lander surface pressure cycle with a Mars general circulation model. J. Geophys. Res. 114 (E07006), 1–19. doi:10.1029/2008JE003302.

Hansen, C.J., Thomas, N., Portyankina, G., McEwen, A., Becker, T., Byrne, S., Herkenhoff, K., Kieffer, H., Mellon, M., 2010. HiRISE observations of gas sublimation-driven activity in Mars' southern polar regions: II. Surficial deposits and their origins. Icarus 205 (1), 283–295. http://doi.org/10.1016/j.icarus.2009.07.021.

Hansen, C.J., McEwen, A., Mellon, M., Portyankina, G., Thomas, N., 2011. Year 3 of HiRISE Observations of Southern Spring on Mars, 42. LPSC Abstract #1651.

Hayne, P.O., Paige, D.A., Heavens, N.G., 2014. The role of snowfall in forming the seasonal ice caps of Mars: models and constraints from the Mars climate sounder. Icarus 231, 122–130. doi:10.1016/j.icarus.2013.10.020.

Hayne, P.O., Paige, D.A., Schofield, J.T., Kass, D.M., Kleinbhl, A., Heavens, N.G., McCleese, D.J., 2012. Carbon dioxide snow clouds on Mars: south polar winter observations by the Mars climate sounder. J. Geophys. Res. E Planets 117, 1–23. doi:10.1029/2011JE004040.

Herkenhoff, K.E., Plaut, J.J., 2000. Surfaceages and resurfacing rates of the polar layered deposits on Mars. Icarus 144, 243–253. doi:10.1006/icar.1999.6287.

Herschel, W., 1784. On the remarkable appearances at the polar regions of the planet Mars, the inclination of its axis, the position of its poles, and its spheroidal figure; with a few hints relating to its real diameter and atmosphere. In: Dreyer, John Louis Emil (Ed.). In: The Scientific Papers of Sir William Herschel, vol. 1. Cambridge University Press, p. 131.

Hess, S.L., Henry, R.M., Tillman, J.E., 1979. The seasonal variation of atmospheric pressure on Mars as affected by the south polar cap. J. Geophys. Res. 84, 2923–2927. doi:10.1029/JB084iB06p02923.

Ingersoll, A.P., 1974. Mars -the case against permanent CO2 frost caps. J. Geophys. Res. 79 (24), 3403–3410. http://doi.org/10.1029/JC079i024p03403.

James, P.B., Kieffer, H.H., Paige, D.A., 1992. The Seasonal Cycle of Carbon Dioxide on Mars. University of Arizona Press, Tucson, Ariz., pp. 934–968. in Mars.

Kieffer, H.H., 2003. Behavior of solid CO_2 on Mars: a real zoo. In: Proceedings of the Sixth International Conference on Mars, pp. 0–3. Retrieved from http://adsabs.harvard.edu/abs/2003mars.conf.3158K.

Kieffer, H.H., 2007. Cold jets in the Martian polar caps. J. Geophys. Res. 112 (E08005), 1–15. doi:10.1029/2006JE002816.

Kieffer, H.H., Christensen, P.R., Titus, T.N., 2006. CO2 jets formed by sublimation beneath translucent slab ice in Mars' seasonal south polar ice cap. Nature 442, 793–796. doi:10.1038/nature04945.

Leighton, R.B., Murray, B.C., 1966. Behavior of carbon dioxide and other volatiles on Mars. Science. http://doi.org/10.1126/science.153.3732.136.

Malin, M.C., 2001. Observational evidence for an active surface reservoir of solid carbon dioxide on Mars. Science 294 (2001), 2146–2148. http://doi.org/10.1126/science.1066416.

Malin, M.C., et al., 2007. Context camera Investigation on board the Mars reconnaissance orbiter. J. Geophys. Res. 112, E05S04. doi:10.1029/2006JE002808.

McEwen, A.S., Eliason, E.M., Bergstrom, J.W., Bridges, N.T., Hansen, C.J., Delamere, W.A., Grant, J.A., Gulick, V.C., Herkenhoff, K.E., Keszthelyi, L., kirk, R.L., Mellon, M.T., Squyres, S.W., Thomas, N., Weitz, C.M., 2007. Mars reconnaissance orbiter's high resolution imaging science experiment (HiRISE). J. Geophys. Res. E Planets 112, 1–40. doi:10.1029/2005JE002605.

Nye, J.F., Durham, W.B., Schenk, P.M., Moore, J.M., 2000. The instability of a south polar cap on Mars composed of carbon dioxide. Icarus 144 (2), 449–455.

Owen, T., Biemann, K., Rushneck, D.R., Biller, J.E., Howarth, D.W., Lafleur, A.L., 1977. The composition of the atmosphere at the surface of Mars. J. Geophys. Res. 82 (28), 4635–4639. http://doi.org/10.1029/JS082i028p04635.

Phillips, R.J., Davis, B.J., Tanaka, K.L., Byrne, S., Mellon, M.T., Putzig, N.E., Seu, R., et al., 2011. Massive CO_2 ice deposits sequestered in the south polar layered deposits of Mars. Science (New York, N.Y.) 332 (6031), 838–841. http://doi.org/10.1126/science.1203091.

Piqueux, S., 2003. Ice cap and the formation of spiders. J. Geophys. Res. 108 (E8), 1–9. http://doi.org/10.1029/2002JE002007.

Piqueux, S., Kleinböhl, A., Hayne, P.O., Kass, D.M., Schofield, J.T., McCleese, D.J., 2015. Variability of the Martian seasonal CO_2 cap extent over eight Mars years. Icarus 251, 164–180. http://dx.doi.org/10.1016/j.icarus.2014.10.045.

Portyankina, G., Markiewicz, W.J., Thomas, N., Hansen, C.J., Milazzo, M., 2010. HiRISE observations of gas sublimation-driven activity in Mars' southern polar regions: III. Models of processes involving translucent ice. Icarus 205, 311–320.

Portyankina, G., Pommerol, A., Aye, K.M., Hansen, C.J., Thomas, N., 2012. Polygonal cracks in the seasonal semi-translucent CO_2 ice layer in Martian polar areas. J. Geophys. Res. E Planets 117 (2), 1–13. http://doi.org/10.1029/2011JE003917.

Sheehan, W., 1996. The Planet Mars: A History of Observation and Discovery. The University of Arizona Press, Tucson Chapter 3.

Smith, D.E., Zuber, M.T., 2011. Volumes of the seasonal polar caps of Mars and implications for density. In: Proceedings of the Fourth International Workshop on the Mars Atmosphere: Modelling and Observation, pp. 285–286.

Smith, D.E., Zuber, M.T., Solomon, S.C., Phillips, R.J., Head, J.W., Garvin, J.B., Duxbury, T.C., et al., 1999. The global topography of Mars and implications for surface evolution. Science 284 (5419), 1495–1503. http://doi.org/10.1126/science.284.5419.1495.

Smith, I.B., Spiga, A., Holt, J.W., 2015. Aeolian processes as drivers of landform evolution at the south pole of Mars. Geomorphology 240, 54–69. http://doi.org/10.1016/j.geomorph.2014.08.026.

Tanaka, K., Kolb, E., Fortezzo, C., 2007. Recent Advances in the stratigraphy of the polar regions of Mars. LPI Contrib. 3–6. Retrieved from http://adsabs.harvard.edu/abs/2007LPICo1353.3276T.

Tanaka, K.L., Skinner, J.a., Dohm, J.M., Irwin, R.P., Kolb, E.J., Fortezzo, C.M., Hare, T.M., et al., 2014. Geologic map of mars. U.S. Geol. Surv. Geol. Invest. 3292. http://doi.org/10.3133/sim3292.

Thomas, N., Portyankina, G., Hansen, C.J., Pommerol, A., 2011. HiRISE observations of gas sublimation-driven activity in Mars' southern polar regions: IV. Fluid dynamics models of CO_2 jets. Icarus 212, 66–85. doi:10.1016/j.icarus.2010.12.016.

Thomas, P.C., Calvin, W., Cantor, B., Haberle, R., James, P.B., Lee, S.W., 2016. Mass balance of Mars' residual south polar cap from CTX images and other data. Icarus 268, 118–130. http://doi.org/10.1016/j.icarus.2015.12.038.

Thomas, P.C., Calvin, W.M., Gierasch, P., Haberle, R., James, P.B., Sholes, S., 2013. Time scales of erosion and deposition recorded in the residual south polar cap of mars. Icarus 225 (2), 923–932. http://doi.org/10.1016/j.icarus.2012.08.038.

Thomas, P.C., James, P.B., Calvin, W.M., Haberle, R., Malin, M.C., 2009. Residual south polar cap of Mars: stratigraphy, history, and implications of recent changes. Icarus 203 (2), 352–375. http://doi.org/10.1016/j.icarus.2009.05.014.

Thomas, P.C., Malin, M.C., James, P.B., Cantor, B.A., Williams, R.M.E., Gierasch, P., 2005. South polar residual cap of Mars: features, stratigraphy, and changes. Icarus 174 (2 SPEC. ISS.), 535–559. http://doi.org/10.1016/j.icarus.2004.07.028.

Titus, T.N. Exposed Water Ice Discovered, 1048(2003), http://doi.org/10.1126/science.1080497.

Wolff, M.J., Clancy, R.T., 2003. Constraints on the size of Martian aerosols from thermal emission spectrometer observations. J. Geophys. Res. 108 (E9), 5097. http://doi.org/10.1029/2003JE002057.

Wolff, M.J., Smith, M.D., Clancy, R.T., Arvidson, R., Kahre, M., Seelos IV, F., Murchie, S., Savijärvi, H., 2009. Wavelength dependence of dust aerosol single scattering albedo as observed by the compact reconnaissance imaging spectrometer. J. Geophys. Res. 114 (6), 1–17. doi:10.1029/2009JE003350.